Efficient numerical schemes for viscoplastic avalanches. Part 2: the 2D case

Enrique D. Fernandez-Nieto, J.M. Gallardo, Paul Vigneaux

Efficient numerical schemes for viscoplastic avalanches. Part 2: the 2D case[☆]

Enrique D. Fernández-Nieto[a], José M. Gallardo[b], Paul Vigneaux[c,d,*]

[a] *Departamento de Matemática Aplicada I, Universidad de Sevilla. E.T.S. Arquitectura. Avda, Reina Mercedes, s/n. 41012 Sevilla, Spain*
[b] *Departamento de Análisis Matemático, Estadística e I. O. y Matemática Aplicada, Universidad de Málaga. F. Ciencias, Campus Teatinos s/n, 29071 Málaga, Spain*
[c] *Unitée de Mathématiques Pures et Appliquées CNRS UMR 5669, Ecole Normale Supérieure de Lyon. 46 allée d'Italie. 69364 Lyon Cedex 07. France*
[d] *Univ. Lyon, INRIA Team NUMED, Ecole Normale Supérieure de Lyon. 46 allée d'Italie. 69364 Lyon Cedex 07. France*

Abstract

This paper deals with the numerical resolution of a shallow water viscoplastic flow model. Viscoplastic materials are characterized by the existence of a yield stress: below a certain critical threshold in the imposed stress, there is no deformation and the material behaves like a rigid solid, but when that yield value is exceeded, the material flows like a fluid. In the context of avalanches, it means that after going down a slope, the material can stop and its free surface has a non-trivial shape, as opposed to the case of water (Newtonian fluid). The model involves variational inequalities associated with the yield threshold: finite volume schemes are used together with duality methods (namely Augmented Lagrangian and Bermúdez-Moreno) to discretize the problem. To be able to accurately simulate the stopping behaviour of the avalanche, new schemes need to be designed, involving the classical notion of well-balancing. In the present context, it needs to be extended to take into account the viscoplastic nature of the material as well as general bottoms with wet/dry fronts which are encountered in geophysical geometries. Here we derive such schemes in 2D as the follow up of the companion paper treating the 1D case. Numerical tests include in particular a generalized 2D benchmark for Bingham codes (the Bingham-Couette flow with *two* non-zero boundary conditions on the velocity) and a simulation of the avalanche path of Taconnaz in Chamonix - Mont-Blanc to show the usability of these schemes on real topographies from digital elevation models (DEM).

Keywords: Viscoplastic, Shallow Water, Finite Volume, Well-Balanced, Variational inequality, Bingham, Taconnaz

1. Introduction

This article is the sequel of the companion paper [10]. It deals with the most general framework for the simulation of viscoplastic (Bingham) avalanches with wet/dry fronts on general 2D bottoms, thanks to a shallow water model discretized with a finite volume method. This approach has several motivations: (i) finite volume methods are used in nearly 40% of the discretizations of geophysical avalanches (40% of the rest being done with finite difference methods) as mentioned in the review [25], (ii) we use the variational inequality framework with duality methods which have proved to be the most accurate for the computation of viscoplastic flows, see [21], (iii) enrichment of geophysical shallow models towards viscoplastic behaviour is increasingly in use to take into account the material ability to rigidify [1, 25, 21], (iv) the prototypical shallow viscoplastic model covered in this paper is well adapted to (wet) dense snow avalanches (by opposition to powder snow avalanches) which are occurring more and more frequently with the global warming of the atmosphere (see [2]).
In the present work, we extend in 2D the 1D schemes developed in [10]. We make a careful study of the ability of the schemes to compute the stationary states of an avalanche. This is done thanks to a coupling between the finite volume method used for the discretization in space and the duality method used to solve the non-Newtonian character of the material. This leads to an extended notion of viscoplastic well-balancing. In this case, we say that the method is well-balanced if it preserves exactly two kinds of stationary solutions: (i) material at rest independently of the rigidity of the material and (ii) rigid enough material with free surface parallel to a reference plane. Let us remark that the latter is more relevant for viscoplastic materials, nevertheless it is necessary to preserve also the first one, material at rest, in order to be consistent with a numerical method for a Newtonian fluid when τ_y tends to zero. We study also the numerical cost and (when possible) the *a priori* estimation of the optimal intrinsic parameter of two duality methods: the augmented Lagrangian (AL) and the Bermúdez-Moreno (BM) methods. Note that the

[☆] This document is an improved version (some misprints corrected) of the published article whose DOI is given below.
[*] Corresponding author
Email addresses: edofer@us.es (Enrique D. Fernández-Nieto), jmgallardo@uma.es (José M. Gallardo), Paul.Vigneaux@math.cnrs.fr (Paul Vigneaux)

schemes proposed here can be extended straightforwardly to power viscoplastic laws (such as Herschel-Bulkley). Several computational tests illustrate the performances of the schemes. First, we consider a 2D Couette geometry for which we propose a generalized analytic solution with two non-zero boundary conditions on the velocity (usual solutions assume that one of the boundary is fixed). This can be a benchmark for testing classic 2D Bingham codes. Second, we study the well-balanced property for rigid materials by considering a complex random bottom on a 30° slope reference plane: the free surface is parallel to the reference plane and has complex wet/dry fronts. Third, we build a numerically demanding 2D academic dam break test on a complex topography where the final stationary solution exhibits strong gradients of the free surface at the wet/dry front. Finally, we show the ability of the schemes to compute the final stationary state of an avalanche on a real topography (given by the ASTER Digital Elevation Model): we used historical data of (frequent) avalanches at the Taconnaz path in the Mont-Blanc, one of the longest sites in Europe with a path close to 7km. This test involves a large computation domain and long physical times with a rich dynamics of the progressive stopping of the avalanche.

In section 2, we recall the model under consideration. In section 3, we derive the 2D versions of the augmented-Lagrangian and the Bermúdez-Moreno methods. For the latter, we give a theoretical a priori estimation of duality parameter which leads to smallest computational time of the duality resolution. This is associated to the computation of the velocity field. We then detail (section 4) the construction and properties of the 2D well-balanced finite volume method for the space discretization. Numerical illustrations are finally presented in section 5.

2. Models

The model problem for viscoplastic shallow flows is naturally the one presented in the first part of this work [10]. We refer to [4] for more details. The geometry is as shown on Figure 1. We consider a fluid domain of height

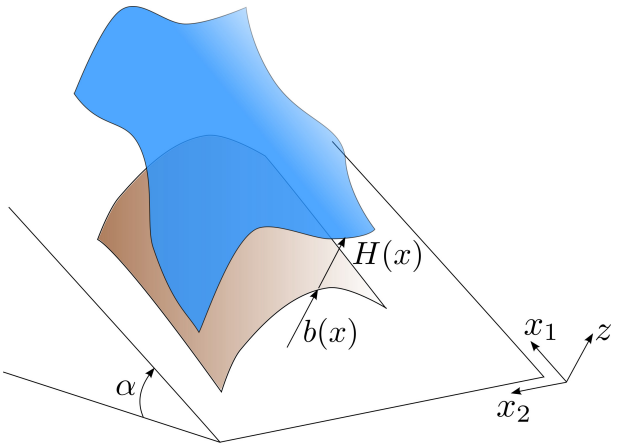

Figure 1: Sketch of the 2D domain and convention for the *local* coordinates. $\boldsymbol{x} = (x_1, x_2)$

H over a general bottom b. More precisely, let $\Omega \subset \mathbb{R}^2$ be a given domain for the space variable $\boldsymbol{x}$. The $\mathbb{R}^2$ plane generated by Ω is supposed to be sloping at an angle α from the horizontal plane. We denote by $z \in \mathbb{R}$ the variable in the orthogonal direction to Ω. The bottom which bounds the fluid by below is defined by $b(\boldsymbol{x}), \boldsymbol{x} \in \Omega$. We denote by $\mathcal{D}(t)$ the fluid domain defined as

$$\mathcal{D}(t) = \{(\boldsymbol{x}, z) \in \Omega \times \mathbb{R} \ / \ b(\boldsymbol{x}) < z < b(\boldsymbol{x}) + H(t, \boldsymbol{x})\}, \tag{1}$$

where H is the time-dependent height of the fluid.

As usual for shallow water type models, we denote by $V = V(t, \boldsymbol{x}) \in \mathbb{R}^2$ the vector of the average of the velocity (orthogonal to the z-axis) along the depth of the fluid (i.e. from $z = b(\boldsymbol{x})$ to $z = b(\boldsymbol{x}) + H(t, \boldsymbol{x})$). We take into account the fact that there may be friction on the bottom through a coefficient β. The fluid undergoes a body force denoted as $(f_\Omega, f_z) \in \mathbb{R}^2 \times \mathbb{R}$ in the $\Omega \times z$ frame of reference. Note that f_Ω and f_z are both assumed to be constant.
Since we are considering a Bingham constitutive law, the material is characterized by a viscosity η and a yield stress τ_y. The latter is associated to the plastic behaviour of the material and this leads (cf. [8]) to a variational inequality for the momentum conservation relation (see equation 4). On the contrary, the conservation of mass is rather classic for this type of integrated model (see equation 3). Given the space

$$\mathcal{V}(t) = \{\Psi \in H^1(\Omega)^2 \ / \ \Psi = 0 \text{ on } \partial\Omega\} := H^1_0(\Omega)^2 \tag{2}$$

and some initial conditions at $t = 0$, the problem is to find $H \in L^2([0,T], L^\infty(\Omega))$, $V \in L^2([0,T]; \mathcal{V}(t))$, with $\partial_t V \in L^2([0,T]; L^2(\Omega)^2)$, such that

$$\partial_t H + \mathrm{div}_{\boldsymbol{x}}(HV) = 0, \tag{3}$$

and

$$\begin{aligned}
&\forall \Psi \in \mathcal{V}(t), \quad \int_\Omega H\Big(\partial_t V + (V\cdot\nabla_{\boldsymbol{x}})V\Big)\cdot(\Psi - V)d\boldsymbol{x} + \int_\Omega \beta V\cdot(\Psi - V)d\boldsymbol{x} \\
&+ \int_\Omega 2\eta H D(V) : D(\Psi - V)d\boldsymbol{x} + \int_\Omega 2\eta H \mathrm{div}_{\boldsymbol{x}} V(\mathrm{div}_{\boldsymbol{x}}\Psi - \mathrm{div}_{\boldsymbol{x}} V)d\boldsymbol{x} \\
&+ \int_\Omega \sqrt{2}\tau_y H\Big(\sqrt{D(\Psi):\, D(\Psi) + (\mathrm{div}_{\boldsymbol{x}}\Psi)^2} - \sqrt{D(V):\, D(V) + (\mathrm{div}_{\boldsymbol{x}} V)^2}\Big)d\boldsymbol{x} \\
&\geq \int_\Omega H(f_\Omega + f_z\nabla_{\boldsymbol{x}} b)\cdot(\Psi - V)d\boldsymbol{x} - \int_\Omega \frac{H^2}{2} f_z(\mathrm{div}_{\boldsymbol{x}}\Psi - \mathrm{div}_{\boldsymbol{x}} V)d\boldsymbol{x},
\end{aligned} \tag{4}$$

where

$$D(U) := \frac{1}{2}\Big[\nabla_{\boldsymbol{x}} U \; + \; (\nabla_{\boldsymbol{x}} U)^t\Big], \tag{5}$$

$$\nabla_{\boldsymbol{x}} U := \left(\frac{\partial U_i}{\partial x_j}\right)_{i,j}, \quad i = 1,2,\; j = 1,2, \tag{6}$$

$$\mathrm{div}_{\boldsymbol{x}} U := \frac{\partial U_1}{\partial x_1} \; + \; \frac{\partial U_2}{\partial x_2}, \qquad \forall\, U(t,\cdot) := (U_1, U_2) \in \mathcal{V}(t). \tag{7}$$

The *shallow water* formulation (4) is in weak form. Note that the derivation of (4) comes from the asymptotic analysis of the integrated 3D equations: this explains why we first present this variational form. From (4), we can then find the strong (i.e. non-variational) form (9)-(10) , which is clearer to read. Obviously, we obtain a Bingham constitutive law but it is modified compared to the canonical law. Indeed, the integration of the 3D equations to the 2D form leads to an *integrated* Bingham law (10) (with corrector terms $\mathrm{tr}(D(V))I$). Let us consider the space $X = \mathbb{R}^{2\times 2}$ with scalar product $(p,q) := (p:\, q + \mathrm{tr}(p)\,\mathrm{tr}(q))$ and associated norm $\|\cdot\|$. That is, for $p \in X$,

$$\|p\| = \sqrt{\sum_{i,j} p_{i,j}^2 + \left(\sum_i p_{i,i}\right)^2}. \tag{8}$$

By using this notation the strong formulation of (4) can be written as follows:

$$H\Big(\partial_t V + (V\cdot\nabla_{\boldsymbol{x}})V\Big) - \mathrm{div}_{\boldsymbol{x}}(H\sigma) = H(f_\Omega + f_z\nabla_{\boldsymbol{x}} b) - \nabla_{\boldsymbol{x}}\left(\frac{H^2}{2} f_z\right) - \beta V, \tag{9}$$

where

$$\begin{cases}
\sigma = 2\eta\,(D(V) + \mathrm{tr}(D(V))I) + \sqrt{2}\tau_y \dfrac{D(V) + \mathrm{tr}(D(V))I}{\|D(V)\|} & \text{if } \|D(V)\| \neq 0 \\
\|\sigma\| \leq \sqrt{2}\tau_y & \text{if } \|D(V)\| = 0.
\end{cases} \tag{10}$$

Let us remark that the $\sqrt{2}$ factor multiplying τ_y appears because of the use of Frobenius norm. Then, the actual formulation is equivalent to the one considering a Eulerian norm.

Note that in the following, the body force will be the influence of gravity, denoted by g. To write this force, we must decide what is the orientation of the plane generated by Ω; by convention we will say that if (x_1, x_2, z) is the frame of reference (cf. Figure 1), then the tilted axis (with respect to the horizontal) is x_1, i.e.

$$f_\Omega = (-g\sin\alpha\,,\, 0), \quad f_z = -g\cos\alpha. \tag{11}$$

Note also that for numerical accuracy, it is often better to consider the simulation of geophysical flows over large domains (like for instance in Section 5.3 for the Taconnaz avalanche path) by rescaling the equations to simulate the flow on a domain of order one length. Namely, we introduce a characteristic horizontal length L_c and vertical height H_c. We then make the following rescaling (denoting $\epsilon = H_c/L_c$):

$$\boldsymbol{x} = L_c\tilde{\boldsymbol{x}},\; z = H_c\tilde{z},\; t = \frac{L_c}{\sqrt{gH_c}}\tilde{t},\; b = H_c\tilde{b},\; V = \sqrt{gH_c}\tilde{V},\; \eta = H_c\sqrt{gH_c}\tilde{\eta},\; \tau_y = \epsilon g H_c\tilde{\tau}_y,\; \beta = \epsilon\sqrt{gH_c}\tilde{\beta},\; f_{\cdot} = g\tilde{f}_{\cdot}. \tag{12}$$

In these new variables (and omitting the tildes), (4) reads:

$$\begin{aligned}
&\forall \Psi \in \mathcal{V}(t), \quad \int_\Omega H\Big(\partial_t V + (V\cdot\nabla_{\boldsymbol{x}})V\Big)\cdot(\Psi - V)d\boldsymbol{x} + \int_\Omega \beta V\cdot(\Psi - V)d\boldsymbol{x} \\
&+ \int_\Omega \epsilon 2\eta H D(V) : D(\Psi - V)d\boldsymbol{x} + \int_\Omega \epsilon 2\eta H \mathrm{div}_{\boldsymbol{x}} V(\mathrm{div}_{\boldsymbol{x}}\Psi - \mathrm{div}_{\boldsymbol{x}} V)d\boldsymbol{x} \\
&+ \int_\Omega \epsilon\sqrt{2}\tau_y H\Big(\|D(\Psi)\| - \|D(V)\|\Big)d\boldsymbol{x} \\
&\geq \int_\Omega H(f_\Omega + f_z\nabla_{\boldsymbol{x}} b)\cdot(\Psi - V)d\boldsymbol{x} - \int_\Omega \frac{H^2}{2} f_z(\mathrm{div}_{\boldsymbol{x}}\Psi - \mathrm{div}_{\boldsymbol{x}} V)d\boldsymbol{x}.
\end{aligned} \tag{13}$$

As most often done in the literature and since the main objective of this work is to treat the viscoplastic discretization difficulty, we consider a first order backward semi-discretization in time. If we denote by Δt the time step, we have from (3)-(4) :

$$\frac{H^{n+1} - H^n}{\Delta t} + \mathrm{div}_{\boldsymbol{x}}(H^n V^n) = 0, \tag{14}$$

and

$$\begin{aligned}
&\int_\Omega H^n\Big(\frac{V^{n+1} - V^n}{\Delta t} + (V^n\cdot\nabla_{\boldsymbol{x}})V^n\Big)\cdot(\Psi - V^{n+1})d\boldsymbol{x} + \int_\Omega \beta V^{n+1}\cdot(\Psi - V^{n+1})d\boldsymbol{x} \\
&+ \int_\Omega 2\eta H^n D(V^{n+1}) : D(\Psi - V^{n+1})d\boldsymbol{x} + \int_\Omega 2\eta H^n \mathrm{div}_{\boldsymbol{x}} V^{n+1}(\mathrm{div}_{\boldsymbol{x}}\Psi - \mathrm{div}_{\boldsymbol{x}} V^{n+1})d\boldsymbol{x} \\
&+ \int_\Omega \sqrt{2}\tau_y H^n\Big(\|D(\Psi)\| - \|D(V^{n+1})\|\Big)d\boldsymbol{x} \\
&\geq \int_\Omega H^n(f_\Omega + f_z\nabla_{\boldsymbol{x}} b)\cdot(\Psi - V^{n+1})d\boldsymbol{x} - \int_\Omega \frac{(H^n)^2}{2} f_z(\mathrm{div}_{\boldsymbol{x}}\Psi - \mathrm{div}_{\boldsymbol{x}} V^{n+1})d\boldsymbol{x}, \quad \forall\Psi.
\end{aligned} \tag{15}$$

Doing so, we see that problems on the height and on the velocity are decoupled. At each time step, supposing that we know (H^n, V^n), we need to solve both problems for (H^{n+1}, V^{n+1}). As in the companion paper [10], we compare two duality methods to handle the variational inequality of the problem on the velocity, namely the Augmented Lagrangian method and Bermúdez-Moreno method. It is the subject of the next section.

3. Duality methods in 2D

3.1. The AL approach

We will extend in 2D the derivation done in [10]. Supposing that (H^n, V^n) are known, the goal is here to solve the problem (15) for V^{n+1}. Using *ad hoc* spaces, variational inequality (15) is now equivalent to a minimization problem

$$\mathcal{J}^n(V^{n+1}) \quad = \quad \min_{V\in\mathcal{V}} \mathcal{J}^n(V), \tag{16}$$

where $\mathcal{J}^n(V) = F^n(B(V)) + G^n(V)$, with $\mathcal{V} = (H_0^1(\Omega))^2$. Let us also denote $\mathcal{H} = L^2(\Omega)^{2\times 2}$,

$$B : \begin{pmatrix} \mathcal{V} & \to & \mathcal{H} \\ V & \mapsto & B(V) = D(V) \end{pmatrix}, \qquad F^n : \begin{pmatrix} \mathcal{H} & \to & \mathbb{R} \\ \lambda & \mapsto & F^n(\lambda) = \int_\Omega \tau_y H^n \|\lambda\| d\boldsymbol{x} \end{pmatrix},$$

and

$$G^n : \mathcal{V} \to \mathbb{R},$$

$$\begin{aligned}
G^n(V) \quad = \quad & \int_\Omega H^n\left(\frac{|V|^2/2 - V^n\cdot V}{\Delta t} + (V^n\cdot\nabla_{\boldsymbol{x}} V^n)\cdot V\right)d\boldsymbol{x} + \int_\Omega \beta\frac{|V|^2}{2}d\boldsymbol{x} \\
& + \int_\Omega \eta H^n\|B(V)\|^2 d\boldsymbol{x} - \int_\Omega H^n\ (f_\Omega + f_z\ \nabla_{\boldsymbol{x}} b)\ \cdot V d\boldsymbol{x} + \int_\Omega f_z\frac{(H^n)^2}{2}\mathrm{div}_{\boldsymbol{x}} V d\boldsymbol{x}.
\end{aligned}$$

In 2D, we define the Lagrangian functional by

$$\mathcal{L}^n : \mathcal{V}\times\mathcal{H}\times\mathcal{H} \to \mathbb{R},$$

$$\mathcal{L}^n(V, q, \mu) = F^n(q) + G^n(V) + \int_\Omega H^n(\mu, B(V) - q)d\boldsymbol{x},$$

and the augmented Lagrangian functional, for a given positive value $r \in \mathbb{R}$, as:

$$\mathcal{L}_r^n(V, q, \mu) = \mathcal{L}^n(V, q, \mu) + \frac{r}{2} \int_\Omega H^n \|B(V) - q\|^2 d\boldsymbol{x}. \tag{17}$$

Again, we determine the saddle point of $\mathcal{L}_r^n(V, q, \mu)$ over $\mathcal{V} \times \mathcal{H} \times \mathcal{H}$ thanks to an augmented Lagrangian algorithm (cf. [11]).

Augmented Lagrangian algorithm (2D)

- **Initialization**: suppose that V^n, H^n and μ^n are known. For $k = 0$, we set $V^k = V^n$ and $\mu^k = \mu^n$.
- **Iterate**:
  - Find $q^{k+1} \in \mathcal{H}$ solution of

$$\mathcal{L}_r^n(V^k, q^{k+1}, \mu^k) \leq \mathcal{L}_r^n(V^k, \underline{q}, \mu^k), \quad \forall \underline{q} \in \mathcal{H}.$$

    In other words, $q^{k+1} \in \mathcal{H}$ is the solution of following minimization problem:

$$\min_{\underline{q} \in \mathcal{H}} \left(\frac{H^n r}{2} \|\underline{q}\|^2 + H^n \sqrt{2}\tau_y \, \|\underline{q}\| - H^n(\mu^k + rB(V^k)) : \underline{q} - H^n \operatorname{tr}(\mu^k + rB(V^k)) \operatorname{tr}(\underline{q}) \right). \tag{18}$$

    And the solution of this problem is computed locally for all $\boldsymbol{x} \in \Omega$:

$$q^{k+1} = \begin{cases} 0 & \text{if } \|\mu^k + rB(V^k)\| < \sqrt{2}\tau_y, \\ \dfrac{1}{r}\left((\mu^k + rB(V^k)) - \sqrt{2}\tau_y \, \dfrac{\mu^k + rB(V^k)}{\|\mu^k + rB(V^k)\|} \right) & \text{otherwise.} \end{cases} \tag{19}$$

  - Find $V^{k+1} \in \mathcal{V}$ solution of

$$\mathcal{L}_r^n(V^{k+1}, q^{k+1}, \mu^k) \leq \mathcal{L}_r^n(V, q^{k+1}, \mu^k), \quad \forall V \in \mathcal{V}.$$

    From (17), by differentiating $\mathcal{L}_r^n(V, q, \mu)$ with respect to V, we deduce that V^{k+1} is the solution of the following linear problem (whose resolution is detailed in Section 4):

$$\begin{aligned} H^n \left(\frac{V^{k+1} - V^n}{\Delta t} \right) + \beta V^{k+1} - (2\eta + r) \left(\operatorname{div}_{\boldsymbol{x}}(H^n D(V^{k+1})) + \nabla_{\boldsymbol{x}}(H^n \operatorname{div}_{\boldsymbol{x}}(V^{k+1})) \right) \\ + H^n (V^n \cdot \nabla_{\boldsymbol{x}} V^n) - (f_\Omega + f_z \, \nabla_{\boldsymbol{x}} b) \, H^n - \nabla_{\boldsymbol{x}} \left(\frac{(H^n)^2}{2} f_z \right) \\ - \operatorname{div}_{\boldsymbol{x}} \left(H^n \left(\mu^k - r q^{k+1} \right) \right) - \nabla_{\boldsymbol{x}} \left(H^n \operatorname{tr}(\mu^k - r q^{k+1}) \right) = 0. \end{aligned} \tag{20}$$

  - Update the Lagrange multiplier via

$$\mu^{k+1} = \mu^k + r \left(B(V^{k+1}) - q^{k+1} \right). \tag{21}$$

  - Check convergence (see below) and update: $V^k = V^{k+1}$, $\mu^k = \mu^{k+1}$, $k = k+1$ and go to the next iteration ...
- ... **until** convergence is reached:

$$\frac{\|\mu^{k+1} - \mu^k\|}{\|\mu^k\|} \leq tol. \tag{22}$$

At convergence, we get the value of V^{n+1} by setting $V^{n+1} = V^{k+1}$ (in the numerical tests presented in this paper, we set $tol = 10^{-5}$). It is also shown in [11] that this algorithm converges to the saddle point of (17).

3.2. The BM approach and its optimal parameter

3.2.1. The BM algorithm

The BM algorithm in the two-dimensional case follows similar guidelines as in [10], once a proper choice of norms is made. In particular, we use the space $\mathcal{V} = H_0^1(\Omega)^2$ endowed with the scalar product

$$(V, W)_{\mathcal{V}} = \int_\Omega D(V) \colon D(W) d\boldsymbol{x} + \int_\Omega \mathrm{div}_{\boldsymbol{x}}(V)\mathrm{div}_{\boldsymbol{x}}(W) d\boldsymbol{x}, \quad V, W \in \mathcal{V}.$$

It readily follows from the arithmetic-geometric mean property and Korn inequality that the associated norm

$$\|V\|_{\mathcal{V}} = \left(\|D(V)\|_{L^2}^2 + \|\mathrm{div}_{\boldsymbol{x}}(V)\|_{L^2}^2\right)^{1/2}$$

verifies $C_K^{-1}\|\nabla V\|_{L^2} \le \|V\|_{\mathcal{V}} \le \sqrt{3}\|\nabla V\|_{L^2}$, where C_K is a Korn constant. Therefore, the norm $\|\cdot\|_{\mathcal{V}}$ is equivalent to the norm $\|\nabla \cdot\|_{L^2}$ in $H_0^1(\Omega)^2$, so $\mathcal{V}$ turns out to be a Hilbert space. In a similar way, the space $\mathcal{H} = L^2(\Omega)^{2\times 2}$ is also a Hilbert space with the scalar product

$$(Z, W)_{\mathcal{H}} = \int_\Omega Z \colon W d\boldsymbol{x} + \int_\Omega \mathrm{tr}(Z)\,\mathrm{tr}(W) d\boldsymbol{x},$$

as the associated norm is equivalent to $\|\cdot\|_{L^2}$. Notice also that $\|V\|_{\mathcal{V}} = \|B(V)\|_{\mathcal{H}}$ for every $V \in \mathcal{V}$.

Consider now the linear operator $A \colon \mathcal{V} \to \mathcal{V}'$ defined as

$$\langle A(V), \Psi\rangle = \int_\Omega \left(\frac{H^n}{\Delta t} + \beta\right) V \cdot \Psi d\boldsymbol{x} + \int_\Omega 2\eta H^n D(V) \colon D(\Psi) d\boldsymbol{x} + \int_\Omega 2\eta H^n \mathrm{div}_{\boldsymbol{x}}(V)\mathrm{div}_{\boldsymbol{x}}(\Psi) d\boldsymbol{x},$$

which is coercive with constant $\gamma = 2\eta H^n_{\min}$ (where $H^n_{\min} = \min H^n(\boldsymbol{x}) > 0$):

$$\langle A(V), V\rangle \ge \left(\frac{H^n_{\min}}{\Delta t} + \beta\right)\|V\|_{L^2}^2 + 2\eta H^n_{\min}\|V\|_{\mathcal{V}}^2 \ge 2\eta H^n_{\min}\|V\|_{\mathcal{V}}^2, \quad \forall\, V \in \mathcal{V}.$$

Define also the functional $j \colon \mathcal{V} \to \mathbb{R}$ given by

$$j(V) = \int_\Omega \sqrt{2}\tau_y H^n \sqrt{|D(V)|^2 + \mathrm{div}_{\boldsymbol{x}}(V)^2} d\boldsymbol{x},$$

and let $L \in \mathcal{V}'$ be

$$\langle L, \Psi\rangle = \int_\Omega \frac{H^n}{\Delta t} V^n \cdot \Psi d\boldsymbol{x} - \int_\Omega H^n V^n \cdot \nabla_{\boldsymbol{x}} V^n \Psi d\boldsymbol{x} + \int_\Omega H^n (f_\Omega + f_z \nabla_{\boldsymbol{x}} b) \cdot \Psi d\boldsymbol{x} - \int_\Omega \frac{(H^n)^2}{2} f_z \mathrm{div}_{\boldsymbol{x}}(\Psi) d\boldsymbol{x}.$$

Then, the variational inequality (15) can be expressed as: Find $V \in \mathcal{V}$ such that

$$\langle A(V), \Psi - V\rangle + j(\Psi) - j(V) \ge \langle L, \Psi - V\rangle, \quad \forall\, \Psi \in \mathcal{V}. \tag{23}$$

Let $\Phi \colon \Omega \times X \to \mathbb{R}$ be the function

$$\Phi(\boldsymbol{x}, p) = \sqrt{2}\tau_y H^n(\boldsymbol{x})\|p\|,$$

and define $T \colon \mathcal{H} \to \mathbb{R}$ as

$$T(Z) = \int_\Omega \Phi(\boldsymbol{x}, Z(\boldsymbol{x})) d\boldsymbol{x}.$$

Using that $\mathrm{div}_{\boldsymbol{x}}(V) = \mathrm{tr}(D(V))$ we have $j(V) = T(B(V))$, where $B \colon \mathcal{V} \to \mathcal{H}$ is given by $B(V) = D(V)$. Now, reasoning as in [10], the variational inequality (23) can be written as: Find $V \in \mathcal{V}$ and $\theta \in \mathcal{H}$ such that

$$\begin{cases} A(V) + \omega B^*(B(V)) + B^*(\theta^k) = L, \\ \theta = G_\lambda^\omega(B(V) + \lambda\theta), \end{cases} \tag{24}$$

where G_λ^ω is the Yosida approximation of $G^\omega = \partial T - \omega I$; the parameters λ and ω are arbitrary positive numbers satisfying $\lambda\omega < 1$. The BM method for (24) reads then as follows: For $k \ge 0$, θ^k being known, compute V^k and θ^{k+1} by solving

$$\begin{cases} A(V^k) + \omega B^*(B(V^k)) + B^*(\theta^k) = L, \\ \theta^{k+1} = G_\lambda^\omega(B(V^k) + \lambda\theta^k). \end{cases} \tag{25}$$

From now on we will assume the condition $\lambda\omega = 1/2$, which ensures the convergence of the BM algorithm and it is also fundamental in the computation of the optimal parameters in Section 3.2.2 (see [10] and the references therein).

Remark 1. *The BM method shares some conceptual properties with the iterative method introduced in [5] (see also [7, Sect. 7.3]). This method is a version of the classical Uzawa's algorithm, which is based on a projection operator on a closed convex set. In the BM algorithm, the projector is substituted by a Yosida approximation, which can be applied in more general contexts. Indeed, when the functional $j(v)$ is the support function of a closed convex set, BM reduces to Uzawa's method.*

Recall that ([9]):

$$\partial T(Z) = \{W \in \mathcal{H} \colon W(\boldsymbol{x}) \in \partial\Phi(\boldsymbol{x}, Z(\boldsymbol{x})) \text{ a.e. } \boldsymbol{x} \in \Omega\}. \tag{26}$$

The subdifferential of T can thus be computed pointwise in terms of the subdifferential of Φ. To this end, remember that we have defined the space $X = \mathbb{R}^{2\times 2}$ with scalar product $(p, q) = (p \colon q + \mathrm{tr}(p)\,\mathrm{tr}(q))$ and associated norm $\|\cdot\|$. Then, define $\phi \colon X \to \mathbb{R}$ as $\phi(p) = c\|p\|$, where c is an arbitrary constant. For $p \neq 0$, the function ϕ is Gâteaux differentiable, so the subdifferential $\partial\phi(p)$ consists only of the gradient:

$$\nabla_{\boldsymbol{x}}\phi(p) = c\frac{p}{\|p\|}.$$

On the other hand, one can see that

$$\partial\phi(0) = \{q \in X \colon \|q\| \leq c\}.$$

Finally, the Yosida approximation G_λ^ω can be computed as follows: for a.e. $\boldsymbol{x} \in \Omega$ and $Z \in \mathcal{H}$,

$$G_\lambda^\omega(Z)(\boldsymbol{x}) = \begin{cases} \dfrac{Z(\boldsymbol{x})}{\lambda} & \text{if } \|Z(\boldsymbol{x})\| \leq \lambda\sqrt{2}\tau_y H^n(\boldsymbol{x}), \\ \dfrac{\sqrt{2}\tau_y H^n(\boldsymbol{x}) - \omega\|Z(\boldsymbol{x})\|}{(1-\lambda\omega)\|Z(\boldsymbol{x})\|} Z(\boldsymbol{x}) & \text{if } \|Z(\boldsymbol{x})\| > \lambda\sqrt{2}\tau_y H^n(\boldsymbol{x}). \end{cases}$$

This expression can be regarded as a generalization of the formula obtained in the one-dimensional case. We notice that

$$\|Z(\boldsymbol{x})\| = \sqrt{Z(\boldsymbol{x}) \colon Z(\boldsymbol{x}) + \mathrm{tr}(Z(\boldsymbol{x}))^2}, \quad \text{a.e. } \boldsymbol{x} \in \Omega,$$

so the following relation holds:

$$\|Z\|_{\mathcal{H}} = \left(\int_\Omega \|Z(\boldsymbol{x})\|^2 d\boldsymbol{x}\right)^{1/2}.$$

We end this section by giving the explicit form of the linear problem to be solved at each iteration of (25). After integration by parts, it can be written as follows (and compared to (20)):

$$H^n\left(\frac{V^{k+1}-V^n}{\Delta t}\right) + \beta V^{k+1} - 2\eta(\mathrm{div}_{\boldsymbol{x}}(H^n D(V^{k+1})) + \nabla_{\boldsymbol{x}}(H^n \mathrm{div}_{\boldsymbol{x}}(V^{k+1}))) - \omega(\mathrm{div}_{\boldsymbol{x}}(D(V^{k+1})) + \nabla_{\boldsymbol{x}}(\mathrm{div}_{\boldsymbol{x}}(V^{k+1})))$$
$$+ H^n(V^n \cdot \nabla_{\boldsymbol{x}} V^n) - (f_\Omega + f_z\,\nabla_{\boldsymbol{x}} b)\,H^n - \nabla_{\boldsymbol{x}}\left(\frac{(H^n)^2}{2} f_z\right) - \mathrm{div}_{\boldsymbol{x}}(\theta^k) - \nabla_{\boldsymbol{x}}(\mathrm{tr}(\theta^k)) = 0. \tag{27}$$

3.2.2. Study of the optimal parameter

The analysis on the optimal choice of parameters performed in [10] can be adapted to the 2D case. First, let $\mathcal{V}_h$ be a finite-dimensional subspace of $\mathcal{V}$ of standard conforming $\mathbb{P}_1$ finite elements, being h the mesh size (dependence on h will be dropped unless necessary). Now, [10, Equation (62)] and [10, Equation (64)] read as

$$\langle A(V^k - V), \Psi\rangle + \omega\,(B(V^k - V), B(\Psi))_{\mathcal{H}} + (\theta^k - \theta, B(\Psi))_{\mathcal{H}} = 0, \quad \forall\,\Psi \in \mathcal{V}_h, \tag{28}$$

and

$$\|\theta^{k+1} - \theta\|_{\mathcal{H}}^2 \leq \|\theta^k - \theta\|_{\mathcal{H}}^2 - 4\omega\langle A(V^k - V), V^k - V\rangle, \tag{29}$$

respectively. Notice that the condition $\lambda\omega = 1/2$ has been assumed.

Let now C_P and C_K be, respectively, the constants in the Poincaré and Korn inequalities (i.e., $\|\Psi\|_{L^2} \leq C_P\|\nabla\Psi\|_{L^2}$ and $\|\nabla\Psi\|_{L^2} \leq C_K\|D(\Psi)\|_{L^2}$, for every $\Psi \in \mathcal{V}_h$), and define $\gamma_1 = C_P^{-1}C_K^{-1}$. Let γ_2 be such that $\|V\|_{\mathcal{V}} \leq \gamma_2\|V\|_{L^2}$ for every $V \in \mathcal{V}_h$. Then, equation (28) implies, for all $\Psi \in \mathcal{V}_h$,

$$(\theta^k - \theta, B(\Psi))_{\mathcal{H}} \leq \left(\frac{H^n_{\max}}{\Delta t} + \beta\right)\|V^k - V\|_{L^2}\|\Psi\|_{L^2} + (\omega + 2\eta H^n_{\max})\|B(V^k - V)\|_{\mathcal{H}}\|B(\Psi)\|_{\mathcal{H}} \leq \Gamma(\omega)\|V^k - V\|_{L^2}\|B(\Psi)\|_{\mathcal{H}},$$

where $H^n_{\max} = \|H^n\|_\infty$ and

$$\Gamma(\omega) = \left(\frac{H^n_{\max}}{\Delta t} + \beta\right)\gamma_1^{-1} + (\omega + 2\eta H^n_{\max})\gamma_2.$$

Assuming that $\Psi \in \mathcal{V}_h$ is such that $B(\Psi) = \theta^k - \theta$, it follows that

$$\|\theta^k - \theta\|_{\mathcal{H}} \leq \Gamma(\omega)\|V^k - V\|_{L^2}.$$

Finally, using the inequality $\|V\|_{\mathcal{V}} \geq \gamma_1\|V\|_{L^2}$ and the coerciveness of A, from (29) we deduce that

$$\|\theta^{k+1} - \theta\|^2_{\mathcal{H}} \leq \mathcal{L}(\omega)\|\theta^k - \theta\|^2_{\mathcal{H}},$$

where

$$\mathcal{L}(\omega) = 1 - 4\omega\gamma\gamma_1^2\Gamma(\omega)^{-2}.$$

Minimization of $\mathcal{L}(\omega)$ leads to the following expression for the optimal parameter ω_{opt}:

$$\omega_{\text{opt}} = \gamma_1^{-1}\gamma_2^{-1}\Big(\frac{H^n_{\max}}{\Delta t} + \beta\Big) + 2\eta H^n_{\max}. \tag{30}$$

It only remains to estimate the constants γ_1 and γ_2. Following [12, Sect. 5.6], the Korn constant can be simply taken as $C_K = \sqrt{2}$. Assuming that the domain Ω is convex, it is known (see [18]) that the optimal choice for C_P is d/π, where d is the diameter of Ω. Thus, $\gamma_1 = \pi/\sqrt{2}d$. On the other hand, we have that $\|V\|_{\mathcal{V}} \leq \sqrt{3}\|\nabla V\|_{L^2} \leq \sqrt{3}\tilde{\gamma}_2\|V\|_{L^2}$ for a certain constant $\tilde{\gamma}_2$, so $\gamma_2 = \sqrt{3}\tilde{\gamma}_2$. Reasoning as in [10, Appendix C], $\tilde{\gamma}_2$ can be taken as $\sqrt{\mu_{\max}}$, where $\mu_{\max}$ is the maximum eigenvalue of the discrete Laplacian problem; in general, this value has to be computed numerically.

Remark 2. *In the particular case of a rectangle* $\Omega = [x_{10}, x_{10}+L_{x_1}]\times[x_{20}, x_{20}+L_{x_2}]$ *with a uniform discretization* $(\Delta x_1, \Delta x_2)$*,* γ_1 *would be*

$$\gamma_1 = \frac{\pi}{\sqrt{2(L^2_{x_1} + L^2_{x_2})}},$$

while γ_2 *could be taken as*

$$\gamma_2 = \sqrt{3\pi^2\Big(\frac{1}{\Delta x_1^2} + \frac{1}{\Delta x_2^2}\Big)}.$$

Note that very recently the FISTA method [23] was introduced for the simulation of viscoplastic flows. It is inspired by proximal gradient methods and allows to speed-up computations, compared to the non-optimized augmented Lagrangian. FISTA could be a complementary approach to the present BM method which has an automatic computation of the optimal duality parameter while giving the same quality results of plastic zones, as the long proven AL method [21].

4. Discretization in space and Well-Balancing in 2D

In this section, we define the spatial discretization for the conservation equation (14) and the velocity equation associated to the iterative algorithm of the AL (equation (20)) and the BM (equation (27)). As mentioned in the companion paper [10] in 1D, there is a rather subtle coupling between both equations through the well-balanced property of the global scheme. This need to be carefully extended when going to the 2D framework.

4.1. Definitions

Note that both equations (20) and (27) can be written under the same structure. Namely, for a time $t = t^n$ and known the velocity at iteration n, V^n, the common system is

$$H^n\frac{V^{k+1}}{\Delta t} + \beta V^{k+1} - \Big(\text{div}_{\boldsymbol{x}}((2\eta H^n + \delta^n)D(V^{k+1})) + \nabla_{\boldsymbol{x}}((2\eta H^n + \delta^n)\text{div}_{\boldsymbol{x}}(V^{k+1}))\Big) =$$

$$H^n\Big(\frac{V^n}{\Delta t} - V^n\cdot\nabla_{\boldsymbol{x}}V^n + (f_\Omega + f_z\,\nabla_{\boldsymbol{x}}(b + H^n))\Big) + \text{div}_{\boldsymbol{x}}(H^n\Pi^k) + \nabla_{\boldsymbol{x}}(\text{tr}(H^n\Pi^k)), \tag{31}$$

where:

- for the AL method:
$$\delta^n = rH^n, \quad \Pi^k = \mu^k - rq^k; \tag{32}$$
- for the BM method:
$$\delta^n = \omega^n, \quad \Pi^k = \theta^k/H^n, \tag{33}$$
where ω^n is defined by the optimal value (30), in terms of H^n.

Let us suppose that the domain Ω is a rectangle, $\Omega = [x_{10}, x_{10} + L_{x_1}] \times [x_{20}, x_{20} + L_{x_2}]$. Let us consider a partition of N_{x_1} intervals of length $\Delta x_1 = L_{x_1}/N_{x_1}$ along x_1; and another partition with N_{x_2} intervals of length $\Delta x_2 = L_{x_2}/N_{x_2}$ along x_2. The 2D mesh is then defined by the union of control volumes

$$\{\mathcal{K}_{i,j}\}_{i=1,\dots,N_{x_1}}^{j=1,\dots,N_{x_2}}, \quad \text{where} \quad \mathcal{K}_{i,j} = [x_{1,i-1/2}, x_{1,i+1/2}] \times [x_{2,j-1/2}, x_{2,j+1/2}], \quad i = 1, \dots, N_{x_1}, \quad j = 1, \dots, N_{x_2},$$

with

$$x_{1,i+1/2} := x_{10} + i\,\Delta x_1, \qquad i = 0, \dots, N_{x_1},$$

$$x_{2,j+1/2} := x_{20} + j\,\Delta x_2, \qquad j = 0, \dots, N_{x_2}.$$

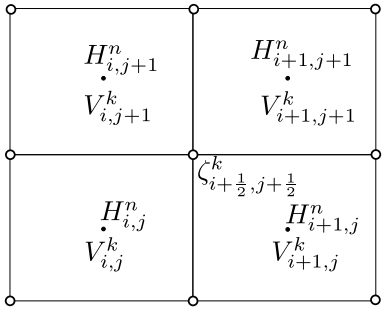

Figure 2: Notations for the discretization

To approximate H^n and V^k, solutions of the semi-discrete system defined by (14)-(31), we consider a finite-volume solver. Then, let us denote at $(x_{1,i}, x_{2,j})$, center of $\mathcal{K}_{i,j}$,

$$H^n_{i,j} \approx \frac{1}{|\mathcal{K}_{i,j}|} \int_{\mathcal{K}_{i,j}} H^n(\boldsymbol{x}) d\boldsymbol{x}, \quad V^k_{i,j} \approx \frac{1}{|\mathcal{K}_{i,j}|} \int_{\mathcal{K}_{i,j}} V^k(\boldsymbol{x}) d\boldsymbol{x}.$$

The *duality multiplier* Π^k is approximated at the vertices of the partition, then let us denote (see figure 2)

$$\Pi^k_{i+1/2,j+1/2} \approx \Pi^k(x_{1,i+1/2}, x_{2,j+1/2}).$$

By the definition of Π^k, equations (32)-(33), we denote

$$\Pi^k_{i+1/2,j+1/2} = \begin{cases} \mu^k_{i+1/2,j+1/2} - r q^k_{i+1/2,j+1/2}, & \text{for } AL, \\ \theta^k_{i+1/2,j+1/2}/H^n_{i+1/2,j+1/2}, & \text{for } BM, \end{cases}$$

and

$$H^n_{i+1/2,j+1/2} = (H^n_{i,j} + H^n_{i+1,j} + H^n_{i,j+1} + H^n_{i+1,j+1})/4. \tag{34}$$

In order to discretize in space the system (14)-(31), we consider a well-balanced finite volume method defined in terms of a diagonal viscosity matrix. This implies that we can present the discretization of the system equation by equation. Nevertheless, their discretizations are not really decoupled because, in order to obtain a well-balanced property, it is necessary to take into account the definition of the *duality multipliers* Π^k in the approximation of the mass conservation equation. Then, we first present the discretization of equation (31) and, second, the discretization of (14).

▹ *Discretization of the velocity equation (31) associated to the iterative algorithm*

Equation (31) is approximated as follows:

$$\left(\frac{H^n_{i,j}}{\Delta t} + \beta\right) V^{k+1}_{i,j} - \mathcal{D}^{k+1}_{i,j} = H^n_{i,j}\left(\frac{V^n_{i,j}}{\Delta t} - \frac{1}{\Delta x_1 \Delta x_2}\left(\Delta x_2(\mathcal{F}^{n-}_{i+1/2,j} + \mathcal{F}^{n+}_{i-1/2,j}) + \Delta x_1(\mathcal{F}^{n-}_{i,j+1/2} + \mathcal{F}^{n+}_{i,j-1/2})\right)\right) + \mathcal{E}^k_{i,j}, \tag{35}$$

where

$$\mathcal{F}^{n\pm}_{i+1/2,j} = \frac{(V_1)^n_{i,j} + (V_1)^n_{i+1,j}}{2}(V^n_{i+1,j} - V^n_{i,j}) - f_\Omega \frac{\Delta x_1}{4} + \frac{f_z}{2}(b_{i+1,j} + H^n_{i+1,j} - b_{i,j} - H^n_{i,j}) \begin{pmatrix} 1 \\ 0 \end{pmatrix} \pm \frac{S_{i+1/2,j}}{2}(V^n_{i+1,j} - V^n_{i,j}),$$

$$\mathcal{F}^{n\pm}_{i,j+1/2} = \frac{(V_2)^n_{i,j} + (V_2)^n_{i,j+1}}{2}(V^n_{i,j+1} - V^n_{i,j}) - f_\Omega \frac{\Delta x_2}{4} + \frac{f_z}{2}(b_{i,j+1} + H^n_{i,j+1} - b_{i,j} - H^n_{i,j}) \begin{pmatrix} 0 \\ 1 \end{pmatrix} \pm \frac{S_{i,j+1/2}}{2}(V^n_{i,j+1} - V^n_{i,j}),$$

being $S_{i+1/2,j}$ and $S_{i,j+1/2}$ the coefficients associated to a finite volume method discretizing the Saint-Venant system with a diagonal viscosity matrix. In this article, we use a Rusanov method, defined by:

$$S_{i+1/2,j} = \left|\frac{V^n_{i,j}+V^n_{i+1,j}}{2}\right| + \sqrt{|f_z|\,\frac{H^n_{i,j}+H^n_{i+1,j}}{2}}, \quad S_{i,j+1/2} = \left|\frac{V^n_{i,j}+V^n_{i,j+1}}{2}\right| + \sqrt{|f_z|\,\frac{H^n_{i,j}+H^n_{i,j+1}}{2}}. \tag{36}$$

The term $\mathcal{E}^k_{i,j} = \mathcal{E}(\Pi^k_{i-1/2,j-1/2}, \Pi^k_{i+1/2,j-1/2}, \Pi^k_{i-1/2,j+1/2}, \Pi^k_{i+1/2,j+1/2})$ is associated to the approximation of $\mathrm{div}_{\boldsymbol{x}}(H^n\Pi^k)+\nabla_{\boldsymbol{x}}(\mathrm{tr}(H^n\Pi^k))$, we set (denoting $[\,\cdot\,]_l$, the l-th component of a vector)

$$\begin{aligned}
\left[\mathcal{E}^k_{i,j}\right]_1 &= \frac{H^n_{i+1/2,j}\left(2(\Pi_{11})^k_{i+1/2,j}+(\Pi_{22})^k_{i+1/2,j}\right) - H^n_{i-1/2,j}\left(2(\Pi_{11})^k_{i-1/2,j}-(\Pi_{22})^k_{i-1/2,j}\right)}{\Delta x_1} \\
&\quad + \frac{H^n_{i,j+1/2}(\Pi_{12})^k_{i,j+1/2} - H^n_{i,j-1/2}(\Pi_{12})^k_{i,j-1/2}}{\Delta x_2}, \\
\left[\mathcal{E}^k_{i,j}\right]_2 &= \frac{H^n_{i,j+1/2}\left(2(\Pi_{22})^k_{i,j+1/2}+(\Pi_{11})^k_{i,j+1/2}\right) - H^n_{i,j-1/2}\left(2(\Pi_{22})^k_{i,j-1/2}-(\Pi_{11})^k_{i,j-1/2}\right)}{\Delta x_2} \\
&\quad + \frac{H^n_{i+1/2,j}(\Pi_{12})^k_{i+1/2,j} - H^n_{i-1/2,j}(\Pi_{12})^k_{i-1/2,j}}{\Delta x_1},
\end{aligned} \tag{37}$$

where we have used the following notations:

$$H^n_{i+1/2,j} = \frac{H^n_{i,j}+H^n_{i+1,j}}{2}, \qquad H^n_{i,j+1/2} = \frac{H^n_{i,j}+H^n_{i,j+1}}{2},$$

$$\Pi^k_{i+1/2,j} = \frac{\Pi^k_{i+1/2,j+1/2}+\Pi^k_{i+1/2,j-1/2}}{2}, \qquad \Pi^k_{i,j+1/2} = \frac{\Pi^k_{i-1/2,j+1/2}+\Pi^k_{i+1/2,j+1/2}}{2}.$$

Finally, the term $\mathcal{D}^{k+1}_{i,j}$ is associated to the discretization of

$$\left(\mathrm{div}_{\boldsymbol{x}}((2\eta H^n+\delta^n)D(V^{k+1})) + \nabla_{\boldsymbol{x}}((2\eta H^n+\delta^n)\mathrm{div}_{\boldsymbol{x}}(V^{k+1}))\right).$$

Let us remark that several possibilities to define the term $\mathcal{D}^{k+1}_{i,j}$ can be considered. Nevertheless, it is necessary to consider a consistent approximation with definition (37), in order to improve the convergence of the iterative algorithm and that the terms depending on the duality parameter cancel for the case $\tau_y = 0$. The following definition is considered:

$$\begin{aligned}
[\mathcal{D}^{k+1}_{i,j}]_1 = \;& 2\Big((2\eta H^n_{i+1/2,j}+\delta^n_{i+1/2,j})\,\Delta_1(V_1^{k+1})|_{i+1/2,j} - (2\eta H^n_{i-1/2,j}+\delta^n_{i-1/2,j})\,\Delta_1(V_1^{k+1})|_{i-1/2,j}\Big)/\Delta x_1^2 \\
&+\Big((2\eta H^n_{i,j+1/2}+\delta^n_{i,j+1/2})\,\Delta_2(V_1^{k+1})|_{i,j+1/2} - (2\eta H^n_{i,j-1/2}+\delta^n_{i,j-1/2})\,\Delta_2(V_1^{k+1})|_{i,j-1/2}\Big)/(2\Delta x_2^2) \\
&+\Big((2\eta H^n_{i+1/2,j}+\delta^n_{i+1/2,j})\,\Delta_2(V_2^{k+1})|_{i+1/2,j} - (2\eta H^n_{i-1/2,j}+\delta^n_{i-1/2,j})\,\Delta_2(V_2^{k+1})|_{i-1/2,j}\Big)/(\Delta x_1\Delta x_2) \\
&+\Big((2\eta H^n_{i,j+1/2}+\delta^n_{i,j+1/2})\,\Delta_1(V_2^{k+1})|_{i,j+1/2} - (2\eta H^n_{i,j-1/2}+\delta^n_{i,j-1/2})\,\Delta_1(V_2^{k+1})|_{i,j-1/2}\Big)/(2\Delta x_1\Delta x_2),
\end{aligned}$$

$$\begin{aligned}
[\mathcal{D}^{k+1}_{i,j}]_2 = \;& 2\Big((2\eta H^n_{i,j+1/2}+\delta^n_{i,j+1/2})\,\Delta_2(V_2^{k+1})|_{i,j+1/2} - (2\eta H^n_{i,j-1/2}+\delta^n_{i,j-1/2})\,\Delta_2(V_2^{k+1})|_{i,j-1/2}\Big)/\Delta x_2^2 \\
&+\Big((2\eta H^n_{i+1/2,j}+\delta^n_{i+1/2,j})\,\Delta_1(V_2^{k+1})|_{i+1/2,j} - (2\eta H^n_{i-1/2,j}+\delta^n_{i-1/2,j})\,\Delta_1(V_2^{k+1})|_{i-1/2,j}\Big)/(2\Delta x_1^2) \\
&+\Big((2\eta H^n_{i+1/2,j}+\delta^n_{i+1/2,j})\,\Delta_2(V_1^{k+1})|_{i+1/2,j} - (2\eta H^n_{i-1/2,j}+\delta^n_{i-1/2,j})\,\Delta_2(V_1^{k+1})|_{i-1/2,j}\Big)/(2\Delta x_1\Delta x_2) \\
&+\Big((2\eta H^n_{i,j+1/2}+\delta^n_{i,j+1/2})\,\Delta_1(V_1^{k+1})|_{i,j+1/2} - (2\eta H^n_{i,j-1/2}+\delta^n_{i,j-1/2})\,\Delta_1(V_1^{k+1})|_{i,j-1/2}\Big)/(\Delta x_1\Delta x_2),
\end{aligned}$$

where,

$$\Delta_1(V_l)|_{i+1/2,j} = \frac{1}{4}\Big((V_l)_{i+1,j+1} + 2(V_l)_{i+1,j} + (V_l)_{i+1,j-1} - (V_l)_{i,j+1} - 2(V_l)_{i,j} - (V_l)_{i,j-1}\Big), \qquad l = 1, 2.$$

$$\Delta_2(V_l)|_{i+1/2,j} = \frac{1}{4}\Big((V_l)_{i,j+1} + (V_l)_{i+1,j+1} - (V_l)_{i,j-1} - (V_l)_{i+1,j-1}\Big),$$

$$\Delta_1(V_l)|_{i,j+1/2} = \frac{1}{4}\Big((V_l)_{i+1,j+1} + (V_l)_{i+1,j} - (V_l)_{i-1,j+1} - (V_l)_{i-1,j}\Big),$$

$$\Delta_2(V_l)|_{i,j+1/2} = \frac{1}{4}\Big((V_l)_{i+1,j+1} + 2(V_l)_{i,j+1} + (V_l)_{i-1,j+1} - (V_l)_{i+1,j} - 2(V_l)_{i,j} - (V_l)_{i-1,j}\Big).$$

Let us denote by $\mathcal{V}^k$ the vector of components $\mathcal{V}^k_l$, for $l = 1, \ldots, 2N_{x_1}N_{x_2}$. Being $(V_1)^k_{i,j} = \mathcal{V}^k_{2(i+(j-1)N_{x_1})-1}$ and $(V_2)^k_{i,j} = \mathcal{V}^k_{2(i+(j-1)N_{x_1})}$, where $V^k_{i,j} = ((V_1)^k_{i,j}, (V_2)^k_{i,j})$, for $i = 1, \ldots, N_{x_1}$ and $j = 1, \ldots, N_{x_2}$. Then, to obtain the values of $\mathcal{V}^{k+1}$, it is necessary to solve the linear system defined by equations (35) for $i = 1, \ldots, N_{x_1}$ and $j = 1, \ldots, N_{x_2}$.

▹ *Well-balanced discretization of the mass conservation equation (14)*

Before to consider the updating of the mass conservation equation, we must previously compute the velocity approximation $\{V^{n+1}_{i,j}\}^{j=1,\ldots,N_{x_2}}_{i=1,\ldots,N_{x_1}}$ by the iterative algorithm corresponding to the AL or the BM method. In particular, when the iterative algorithm has converged, this also gives the value of multipliers $\{\Pi^{\bar{k}}_{i+1/2,j+1/2}\}^{j=0,\ldots,N_{x_2}}_{i=0,\ldots,N_{x_1}}$, being $\bar{k}$ the last iteration of the algorithm.

We consider the following well-balanced finite-volume discretization:

$$H^{n+1}_{i,j} = H^n_{i,j} - \frac{\Delta t}{\Delta x_1}(\phi^n_{i+1/2,j} - \phi^n_{i-1/2,j}) - \frac{\Delta t}{\Delta x_2}(\phi^n_{i,j+1/2} - \phi^n_{i,j-1/2}), \tag{38}$$

where

$$\phi^n_{i+1/2,j} = \frac{H^n_{i+1,j}V^n_{i+1,j} + H^n_{i,j}V^n_{i,j}}{2} - \frac{1}{2}S_{i+1/2,j}(H^n_{i+1,j} - H^n_{i,j} - \mathcal{G}^n_{i+1/2,j}), \tag{39}$$

and analogously

$$\phi^n_{i,j+1/2} = \frac{H^n_{i,j+1}V^n_{i,j+1} + H^n_{i,j}V^n_{i,j}}{2} - \frac{1}{2}S_{i,j+1/2}(H^n_{i,j+1} - H^n_{i,j} - \mathcal{G}^n_{i,j+1/2}). \tag{40}$$

For (38)-(40) to be well-balanced (as proved in section 4.3), the key point is to build in $\mathcal{G}^n_{\cdot,\cdot}$ a discrete approximation of the $\mathrm{div}_{\boldsymbol{x}}(.) + \nabla_x(\mathrm{tr}(.))$ operator acting on the duality corrector $\Pi^{\bar{k}} + D(V^{\bar{k}})$. This follows the insight of the 1D study (see [10]) but the construction is more intricate. We introduce progressively the following quantities, computed from the available discrete variables. First, we define:

$$(\xi_{11})^k_{i+1/2,j+1/2} := (\Pi_{11})^k_{i+1/2,j+1/2} + \frac{\delta^k_{i+1/2,j+1/2}}{2H^n_{i+1/2,j+1/2}\Delta x_1}[V^{n+1}_{i+1,j+1} + V^{n+1}_{i+1,j} - V^{n+1}_{i,j+1} - V^{n+1}_{i,j}]_1, \tag{41}$$

$$(\xi_{22})^k_{i+1/2,j+1/2} := (\Pi_{22})^k_{i+1/2,j+1/2} + \frac{\delta^k_{i+1/2,j+1/2}}{2H^n_{i+1/2,j+1/2}\Delta x_2}[V^{n+1}_{i,j+1} + V^{n+1}_{i+1,j+1} - V^{n+1}_{i,j} - V^{n+1}_{i+1,j}]_2, \tag{42}$$

$$\begin{aligned}(\xi_{12})^k_{i+1/2,j+1/2} := (\Pi_{12})^k_{i+1/2,j+1/2} + \frac{\delta^k_{i+1/2,j+1/2}}{4H^n_{i+1/2,j+1/2}} \Bigg(&\frac{[V^{n+1}_{i+1,j+1} + V^{n+1}_{i+1,j} - V^{n+1}_{i,j+1} - V^{n+1}_{i,j}]_2}{\Delta x_1} \\ &+ \frac{[V^{n+1}_{i,j+1} + V^{n+1}_{i+1,j+1} - V^{n+1}_{i,j} - V^{n+1}_{i+1,j}]_1}{\Delta x_2}\Bigg),\end{aligned} \tag{43}$$

where, following (32)-(33) and using (34), we set

$$\delta^k_{i+1/2,j+1/2} := \begin{cases} rH^n_{i+1/2,j+1/2} & \text{for AL,} \\ \omega^n = \omega_{opt}(H^n_{i+1/2,j+1/2}) & \text{for BM.} \end{cases}$$

Then, we compute these quantities at the center of the edges of control volumes (where the flux is needed). For $l \in 1, 2$ we denote

$$(\xi_{ll})^k_{i+1/2,j} = \frac{(\xi_{ll})^k_{i+1/2,j+1/2} + (\xi_{ll})^k_{i+1/2,j-1/2}}{2}, \qquad (\xi_{ll})^k_{i,j+1/2} = \frac{(\xi_{ll})^k_{i+1/2,j+1/2} + (\xi_{ll})^k_{i-1/2,j+1/2}}{2}.$$

Let us also denote by η the free surface level computed from the reference plane,

$$\eta^n_{i,j} = b_{i,j} + H^n_{i,j} := b(\boldsymbol{x}_{i,j}) + H^n_{i,j}.$$

We are now able to write our definition of the correction terms $\mathcal{G}^n_{i+1/2,j}$ and $\mathcal{G}^n_{i,j+1/2}$, in terms of the aforementioned quantities:

$$\begin{aligned}\mathcal{G}^n_{i+1/2,j} = &\frac{[f_\Omega]_1}{f_z}\Delta x_1 + (b_{i+1,j} - b_{i,j}) + \frac{1}{H^n_{i+1/2,j} f_z}\left(H^n_{i+1/2,j+1/2}(\xi_{12})^{\bar{k}}_{i+1/2,j+1/2} - H^n_{i+1/2,j-1/2}(\xi_{12})^{\bar{k}}_{i+1/2,j-1/2}\right)\frac{\Delta x_1}{\Delta x_2}\\
&+\mathcal{Z}\Big(H^n_{i-1/2,j}\left(2(\xi_{11})^{\bar{k}}_{i-1/2,j} + (\xi_{22})^{\bar{k}}_{i-1/2,j}\right), H^n_{i+1/2,j}\left(2(\xi_{11})^{\bar{k}}_{i+1/2,j} + (\xi_{22})^{\bar{k}}_{i+1/2,j}\right), H^n_{i+3/2,j}\left(2(\xi_{11})^{\bar{k}}_{i+3/2,j} + (\xi_{22})^{\bar{k}}_{i+3/2,j}\right),\\
&\eta^n_{i-1,j}, \eta^n_{i,j}, \eta^n_{i+1,j}, \eta^n_{i+2,j}\Big)\frac{1}{H^n_{i+1/2,j} f_z},\end{aligned}$$

$$\begin{aligned}\mathcal{G}^n_{i,j+1/2} = &\frac{[f_\Omega]_2}{f_z}\Delta x_2 + (b_{i,j+1} - b_{i,j}) + \frac{1}{H^n_{i,j+1/2} f_z}\left(H^n_{i+1/2,j+1/2}(\xi_{12})^{\bar{k}}_{i+1/2,j+1/2} - H^n_{i-1/2,j+1/2}(\xi_{12})^{\bar{k}}_{i-1/2,j+1/2}\right)\frac{\Delta x_2}{\Delta x_1}\\
&+\mathcal{Z}\Big(H^n_{i,j-1/2}\left((\xi_{11})^{\bar{k}}_{i,j-1/2} + 2(\xi_{22})^{\bar{k}}_{i,j-1/2}\right), H^n_{i,j+1/2}\left((\xi_{11})^{\bar{k}}_{i,j+1/2} + 2(\xi_{22})^{\bar{k}}_{i,j+1/2}\right), H^n_{i,j+3/2}\left((\xi_{11})^{\bar{k}}_{i,j+3/2} + 2(\xi_{22})^{\bar{k}}_{i,j+3/2}\right),\\
&\eta^n_{i,j-1}, \eta^n_{i,j}, \eta^n_{i,j+1}, \eta^n_{i,j+2}\Big)\frac{1}{H^n_{i,j+1/2} f_z},\end{aligned}$$

where again $[\,\cdot\,]_l$ is the l-th component of a vector.
To define $\mathcal{Z}$, we use a combination of a second order approximation and a first order upwind approximation via a flux limiter, (see [10]):

$$\mathcal{Z}(d_l, d_c, d_r, s_{-1}, s_0, s_1, s_2) = \chi\,\frac{d_r - d_l}{2} + (1-\chi)\overline{\Delta d}_1, \tag{44}$$

with

$$\overline{\Delta d}_1 = \begin{cases} d_c - d_l & \text{if } s_0 < s_1,\\ d_r - d_c & \text{if } s_0 > s_1,\\ (d_r - d_l)/2 & \text{if } s_0 = s_1.\end{cases}$$

This definition of $\mathcal{Z}$ introduces an upwinding in the discretization of the normal (to the edge of the control volume) variation of the multiplier Π, in the cases of high variations of the free surface. Note that the variations of the multiplier are also related to the pressure gradient, and as a consequence to the free surface. If in the numerical tests we do not have high gradients of the free surface a simple centered difference could be used, as:

$$\mathcal{Z}(d_l, d_c, d_r, s_{-1}, s_0, s_1, s_2) = \frac{d_r - d_l}{2}.$$

The term $\chi = \chi(v(s_{-1}, s_0, s_1, s_2))$ is a flux limiter function with $v(s_{-1}, s_0, s_1, s_2) \in [0, 1]$,

$$v = \max(0, \min(1, \tilde{v})), \qquad \tilde{v} = \begin{cases} \dfrac{3(s_0 - s_{-1})}{s_2 - s_{-1}}, & \text{if } s_1 > s_0,\\[2ex] \dfrac{3(s_2 - s_1)}{s_2 - s_{-1}}, & \text{if } s_1 < s_0,\\[2ex] 1 & \text{if } s_1 = s_0 \text{ or } s_2 = s_{-1}.\end{cases}$$

In [10] has been proposed the following definition of the flux limiter:

$$\chi(v) = 1 - (1 - v^{1/4})^4.$$

Remark 3.

The terms $(\xi_{lm})^k_{i+1/2,j+1/2}$, $l, m = 1, 2$, defined by (41)-(43), have been considered only in the evaluation of the correction terms $\mathcal{G}^n_{i+1/2,j}$ and $\mathcal{G}^n_{i,j+1/2}$. These terms allow us to obtain a scheme verifying the well-balanced properties described in Theorem 1.

Let us remark that we can obtain the same well-balanced properties of the schemes if we set $(\xi_{lm})^k_{i+1/2,j+1/2} = (\Pi_{lm})^k_{i+1/2,j+1/2}$. That is, if we neglect the terms depending on the velocity in the definitions (41)-(43). Nevertheless, these terms are necessary for stability purposes. If we do not include these terms then the CFL condition depends on the parameter of the duality method: the CFL being more restrictive for bigger values of $\{r, \omega\}$.

The correction terms $\mathcal{G}^n_{i+1/2,j}$ and $\mathcal{G}^n_{i,j+1/2}$ are defined as the sum of four terms. The first one takes into account the slope of the reference plane; the second one, the slope of the local topography; the third one, the tangential variation of the multiplier Π on the edge. And the last one, the normal variation to the edge of the multiplier. Note that to preserve general 2D stationary solutions is extremely more complicated than in the 1D case. The proposed definition of the third and fourth terms allows to preserve stationary solutions with a general shape of the free surface with good accuracy (as shown in the numerical tests).

Remark 4. *On the treatment of wet/dry fronts*

It is actually done as the natural extension in 2D of the treatments proposed in the companion paper [10]. For sake of brevity, they are not redescribed here.

4.2. The global coupled scheme

Capitalizing on the previous sections, the description of the global coupled scheme for (14)-(15) can be described in a few words. This global structure is actually the same as for the 1D case [10]. Only the update of the duality variable is more involved due to the tensorial nature of $D(V)$; however, the "dual" localization of V (at $(x_{1,i}, x_{2,j})$) and the duality variables (at $(x_{1,i+1/2}, x_{2,j+1/2})$) allows to compute the gradient in a natural way with centered differentiation. In brief, the global scheme for both AL and BM is the following:

- Initialization at time $t = 0$, $n = 0$, V^n and H^n are given by the initial conditions
- Time loop:
  - Resolution of V^{n+1}:
    - Initialization of the duality loop
    - Duality loop:
      - Resolution of V^{k+1}: this is a linear system coming from the discretization presented in the previous section
      - Update of the duality multipliers. A discretization is needed for equations (19), (21) for the AL method and for the second equation of (25) for the BM method. In order to discretize these equations, we just need to specify $B(V^k)|_{i+1/2,j+1/2}$, approximation of $B(V^k)|_{(x_{1,i+1/2},x_{2,j+1/2})}$. We consider the following discretization for the three components of this symmetric tensor:

$$\begin{aligned}
\left[B(V^k)|_{i+1/2,j+1/2}\right]_{11} &= \frac{1}{2\Delta x_1}\left[V^k_{i+1,j+1} + V^k_{i+1,j} - V^k_{i,j+1} - V^k_{i,j}\right]_1,\\
\left[B(V^k)|_{i+1/2,j+1/2}\right]_{12} &= \frac{1}{4\Delta x_1}\left[V^k_{i+1,j+1} + V^k_{i+1,j} - V^k_{i,j+1} - V^k_{i,j}\right]_2\\
&\quad + \frac{1}{4\Delta x_2}\left[V^k_{i,j+1} + V^k_{i+1,j+1} - V^k_{i,j} - V^k_{i+1,j}\right]_1,\\
\left[B(V^k)|_{i+1/2,j+1/2}\right]_{22} &= \frac{1}{2\Delta x_2}\left[V^k_{i,j+1} + V^k_{i+1,j+1} - V^k_{i,j} - V^k_{i+1,j}\right]_2,
\end{aligned}$$

    - At convergence: $V^{n+1} \leftarrow V^{k+1}$
  - Resolution of H^{n+1}: it is an explicit computation using the discretization presented in the previous section and using the last duality multiplier coming from the computation of V^{n+1} just above.

4.3. Well-balanced properties

Theorem 1. *Let us consider the following initialization of the components of* $\{(\Pi^0)_{i+1/2,j+1/2}\}_{i=0,\dots,N_{x_1}}^{j=0,\dots,N_{x_2}}$,

$$(\Pi^0_{11})_{i+1/2,j+1/2} = -2(\Pi^0_{22})_{i+1/2,j+1/2}, \qquad (\Pi^0_{12})_{i+1/2,j+1/2} = 0, \tag{45}$$

and $(\Pi^0_{22})_{i+1/2,j+1/2}$ *is defined recursively as follows:*

• *for* $j = 0$*:* $i \in \{0, \dots, N_{x_1}\}$

$$(\Pi^0_{22})_{i+1/2,1/2} = \left([f_\Omega]_1\Delta x_1 + f_z(b_{i+1,1} + H^0_{i+1,1} - b_{i,1} - H^0_{i,1})\right)\frac{1}{3H^0_{i+1/2,1}}\left(\sum_{k=1}^{i} H^0_{k,1} - C\right),$$

• *for* $j = 1, \dots, N_{x_2}$*:* $i \in \{0, \dots, N_{x_1}\}$

$$(\Pi^0_{22})_{i+1/2,j+1/2} = \left([f_\Omega]_1 \Delta x_1 + f_z(b_{i+1,j+1/2} + H^0_{i+1,j+1/2} - b_{i,j+1/2} - H^0_{i,j+1/2})\right) \frac{2}{3H^0_{i+1/2,j}} \left(\sum_{k=1}^{i} H^0_{k,j} - C \right) - (\Pi^0_{22})_{i+1/2,j-1/2}, \tag{46}$$

for any constant C*. Particularly, we can set* $C = \sum_{i=1,N_{x_1}/2}^{j=1,N_{x_2}/2} H^0_{i,j}$.

The proposed scheme verifies that if we set this initial value: $(\Pi)^0_{i+1/2,j+1/2} = (\Pi^0)_{i+1/2,j+1/2}$ *(*$\forall\, i,\ j$*), then it preserves exactly two kinds of solutions at rest:*

(i) Material at rest with horizontal free surface*, defined by the initial conditions:*

$$V^0_{i,j} = 0, \quad (x_1)_{i,j} \sin\alpha + (b_{i,j} + H^0_{i,j}) \cos\alpha = \eta,$$

being η *a constant value, corresponding to the level of the free surface.*

(ii) Material at rest with free surface parallel to the plane of reference*, defined by the initial conditions:*

$$V^0_{i,j} = 0, \quad b_{i,j} + H^0_{i,j} = c, \tag{47}$$

begin c *a constant value —the distance from the free surface to the plane of reference—, if the material is rigid enough, i.e. if* τ_y *verifies:*

$$\|\Pi^0_{i+1/2,j+1/2}\| \leq \sqrt{2}\tau_y \quad \forall\, i,\ j. \tag{48}$$

Proof

(i) In this case, the initialization of the multipliers is zero, then it is equivalent to prove that the proposed finite volume method preserves exactly water at rest, which is a classical result and can be proven easily. So, for the purpose of brevity we omit the details.
(ii) In this case, let us divide the proof into two steps: to prove that the velocity remains null and that the height does not change in the time loop.

[Step 1] Let us prove that the velocity remains zero.

First, note that, by (19)-(21) and (25), condition (48) implies that in both cases, for AL and BM methods, the given initialization of the multipliers remains constant in the iterative process. That is,

$$\Pi^k_{i+1/2,j+1/2} = \Pi^0_{i+1/2,j+1/2}, \forall k.$$

As $V^k_{i,j} = 0$ is the solution of the linear system defined by (35), it is enough to prove that the right hand side of the linear system is null. By using that the initial condition verifies (47), the right hand side of the linear system is:

$$f_\Omega H^0_{i,j} + \mathcal{E}^k_{i,j}.$$

Where, by (37), (35) and using (45), we have:

$$\mathcal{E}^k_{i,j} = \begin{pmatrix} -3\dfrac{H^0_{i+1/2,j}(\Pi_{22})^k_{i+1/2,j} - H^0_{i-1/2,j}(\Pi_{22})^k_{i-1/2,j}}{\Delta x_1} \\ 0 \end{pmatrix}, \tag{49}$$

By using (46), and that $b_{i,j} + H^n_{i,j} = c$, we obtain

$$(\Pi_{22})^k_{i+1/2,j} = (\Pi_{22})^0_{i+1/2,j} = \frac{(\Pi_{22})^0_{i+1/2,j+1/2} + (\Pi_{22})^0_{i+1/2,j-1/2}}{2} = [f_\Omega]_1 \Delta x_1 \frac{2}{3H^0_{i+1/2,j}} \left(\sum_{k=1}^{i} H^n_{k,j} - C \right). \tag{50}$$

Then,

$$-3\frac{H^0_{i+1/2,j}(\Pi_{22})^k_{i+1/2,j} - H^0_{i-1/2,j}(\Pi_{22})^k_{i-1/2,j}}{\Delta x_1} = -H^0_{i,j}[f_\Omega]_1.$$

and, as a consequence, we obtain

$$f_\Omega H^0_{i,j} + \mathcal{E}^k_{i,j} = 0.$$

[Step 2] Finally, we prove that the height remains constant. By (38)-(40), it is enough to prove that the terms multiplying the numerical viscosity coefficients $S_{i+1/2,j}$ and $S_{i,j+1/2}$ are zero, i.e. to prove:

$$H^0_{i+1,j} - H^0_{i,j} - \mathcal{G}^n_{i+1/2,j} = 0, \qquad \text{and} \qquad H^0_{i,j+1} - H^0_{i,j} - \mathcal{G}^0_{i,j+1/2} = 0.$$

First, by using (45) and that the stationary solution verifies $b_{i,j} + H^0_{i,j} = c$, we obtain

$$H^0_{i+1,j} - H^0_{i,j} - \mathcal{G}^0_{i+1/2,j} = \frac{[f_\Omega]_1}{f_z}\Delta x_1 + \frac{1}{f_z H_{i+1/2,j}}\mathcal{Z}\Big(-3H^0_{i-1/2,j}(\xi_{22})^0_{i-1/2,j}, -3H^0_{i+1/2,j}(\xi_{22})^0_{i+1/2,j}, -3H^0_{i+3/2,j}(\xi_{22})^0_{i+3/2,j}, c, c, c, c\Big). \tag{51}$$

Moreover, if we consider a centered approximation of $\mathcal{Z}$ or definition (44), we obtain

$$\mathcal{Z}\Big(-3H^0_{i-1/2,j}(\xi_{22})^0_{i-1/2,j}, -3H^0_{i+1/2,j}(\xi_{22})^0_{i+1/2,j}, -3H^0_{i+3/2,j}(\xi_{22})^0_{i+3/2,j}, c, c, c, c\Big) = \frac{-3H^0_{i+3/2,j}(\xi_{22})^0_{i+3/2,j} + 3H^0_{i-1/2,j}(\xi_{22})^0_{i-1/2,j}}{2}.$$

As the velocity is zero, we obtain

$$(\xi_{22})^0_{i+1/2,j} = (\Pi_{22})^0_{i-1/2,j}, \quad \forall i, j$$

Then, using (50), we obtain

$$H^0_{i+1/2,j}(\xi_{22})^0_{i+1/2,j} = [f_\Omega]_1 \Delta x_1 \frac{2}{3}\left(\sum_{k=1}^{i} H^0_{k,j} - C\right).$$

As a consequence,

$$\frac{-3H^0_{i+3/2,j}(\xi_{22})^0_{i+3/2,j} + 3H^0_{i-1/2,j}(\xi_{22})^0_{i-1/2,j}}{2} = -[f_\Omega]_1 \Delta x_1 H_{i+1/2,j}.$$

Then, by using (51),

$$H^n_{i+1,j} - H^n_{i,j} - \mathcal{G}^n_{i+1/2,j} = 0.$$

Secondly, by using also (45) and that the stationary solution verifies $b_{i,j} + H^n_{i,j} = c$, we obtain

$$H^n_{i,j+1} - H^n_{i,j} - \mathcal{G}^n_{i,j+1/2} = \frac{[f_\Omega]_2}{f_z}\Delta x_2 + \frac{1}{f_z H_{i,j+1/2}}\mathcal{Z}\Big(0, 0, 0, c, c, c, c\Big). \tag{52}$$

As $\mathcal{Z}\Big(0, 0, 0, c, c, c, c\Big) = 0$ and $[f_\Omega]_2 = 0$, then,

$$H^n_{i,j+1} - H^n_{i,j} - \mathcal{G}^n_{i,j+1/2} = 0,$$

which concludes the proof. □

5. Numerical tests

As a preliminary test, we must check that the 2D "kernel" Bingham solver of a duality loop is accurate. To do so, it is interesting to note that our model degenerates to the viscoplastic version of the Couette problem for the Stokes equations on V (which could be called the Bingham-Couette problem), i.e. the flow between two concentric rotating cylinders. In Rheology (when one cylinder is fixed and the other is moving), this very classical problem is also known as the "Reiner & Riwlin" test, who gave an analytic solution in this case [20]. In Appendix A, we give a generalized analytic solution of the Bingham-Couette problem in the case where both cylinders are moving (which degenerate to [20] when one cylinder is fixed). We then show that our 2D code with the aforementioned discretizations recovers perfectly the 3 types of existing solutions for V. Note that this test is a good benchmark for any 2D Stokes-Bingham code in which boundary conditions are prescribed in terms of V. We now present tests which take into account both H and V.

5.1. Well-balanced test on stochastic bottom

In this first test, we consider a bottom defined as a random perturbation of a parabolic bottom over a Ω-plane with an angle $\alpha = 30°$. And the free surface is parallel to the reference plane as shown in Figure 3. The random perturbation is considered at each point of the mesh, which has been set to 100^2 points in the domain $[0, 1] \times [0, 1]$. The initial condition is defined as follows:

$$H(\boldsymbol{x}, 0) = \max(6 - b(\boldsymbol{x}), 0) \quad \text{with} \quad b(\boldsymbol{x}) = 4e^{-\tilde{r}} + 15\left((x_1 - 0.5)^2 + (x_2 - 0.5)^2\right),$$

being $\tilde{r}$ a random number between 0 and 1. We see in Figure 3 that this leads to complex wet/dry fronts. We set $\eta = 10^{-3}\ m^2.s^{-1}$, $\beta = 10^{-3}\ m.s^{-1}$ and $g = 9.81\ m.s^{-2}$. For τ_y, one can take any value greater than the smallest one ensuring that condition (48) is fulfilled.

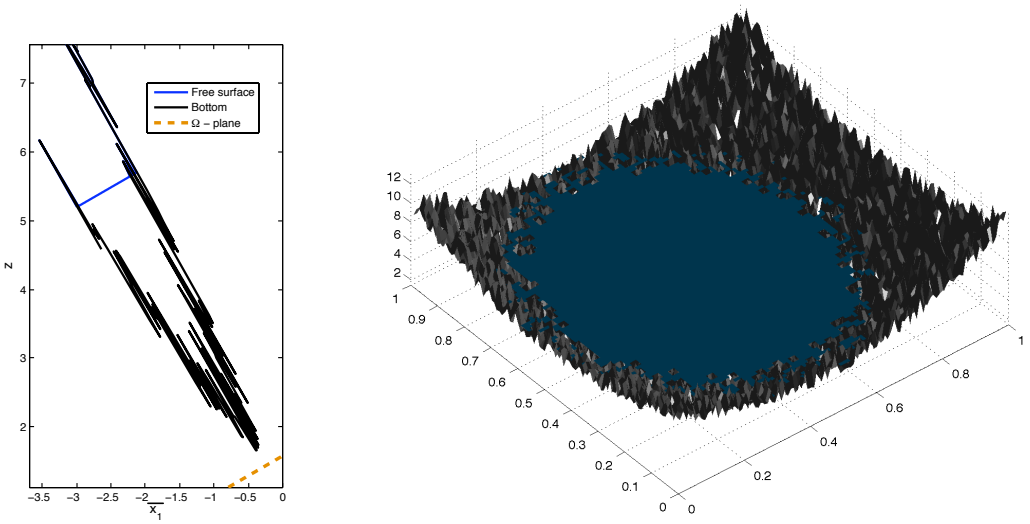

Figure 3: Left: slice of the bottom and the free surface at $x_2 = 0.5$ in *global coordinates* (meaning that $\overline{x_1}$ is obtained via the rotation associated to the angle α, see Fig. 1). Right: bottom $b(\boldsymbol{x})$ (in black) and initial condition $b + H$ (blue), in *local* coordinates.

If we consider the initialization of the multiplier defined in Theorem 1, the stationary solution is preserved up to machine precision for a value of τ_y verifying condition (48). For sake of conciseness we do not show the illustrations here.

In the present test, we instead initialize the multipliers to zero. The simulation is done from $t = 0$ to 1. Actually, at the first time iteration, the multipliers converge (inside the duality loop) to some function which then remains unchanged along the subsequent time iterations. As in 2D the multiplier is (intricately) not uniquely defined, it is not assured that the iterative algorithm converges to the one defined by (45)-(46), which ensures the exact well-balanced property. Nevertheless, we can see numerically that both AL & BM schemes still preserve the stationary solution with a good accuracy. In Figure 4, the multiplier to which the algorithm converges is plotted for illustration (this is done with the BM method but the results are the same with the AL algorithm). We obtain that the time averaged L^2 error for $t \in [0, 1]$ is 6.3×10^{-4} for H and 1.4×10^{-8} for the velocity norm. The averaged difference between $H(x, t)$ and the initial condition, for $t \in [0, 1]$, is represented in Figure 5, together with the averaged norm of the velocity (also for $t \in [0, 1]$).

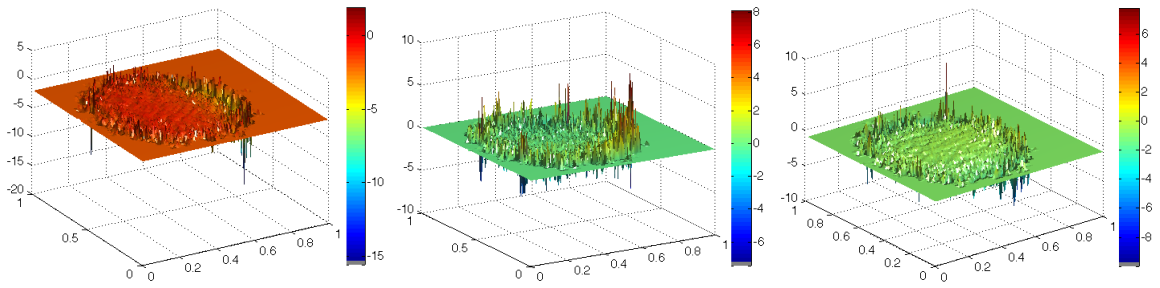

Figure 4: Multiplier at $t = 1$. Left: Π^k_{11}, center: Π^k_{12}, right: Π^k_{22}, being k the last iteration of the duality algorithm.

5.2. *Well-balanced test on academic avalanche*

This test is a dam break simulation where the Ω-plane is sloping at $\alpha = 20°$ and the bottom with two obstacles is defined as follows on $[0; 1]^2$ (cf. Figure 6):

$$b(\boldsymbol{x}) = 1.5\mathrm{e}^{-[20(x_1-0.75)]^4} + 6\mathrm{e}^{-[5(x_1-1.25)]^4} + 3\mathrm{e}^{-[10(x_1-0.5)]^2-[18(x_2-0.5)]^2} + \Big(10(x_2-0.5)^2+1\Big)1.1\mathrm{e}^{-0.9x_1} + 1.1e^{-9x_1}. \quad (53)$$

As initial condition, we set $V \equiv 0$ and (see Figure 6)

$$H(\boldsymbol{x}) = \begin{cases} 10 - b(\boldsymbol{x}) & \text{if } (x_1, x_2) \in [0.7; 0.89] \times [0.4; 0.6], \\ 0 & \text{otherwise .} \end{cases} \quad (54)$$

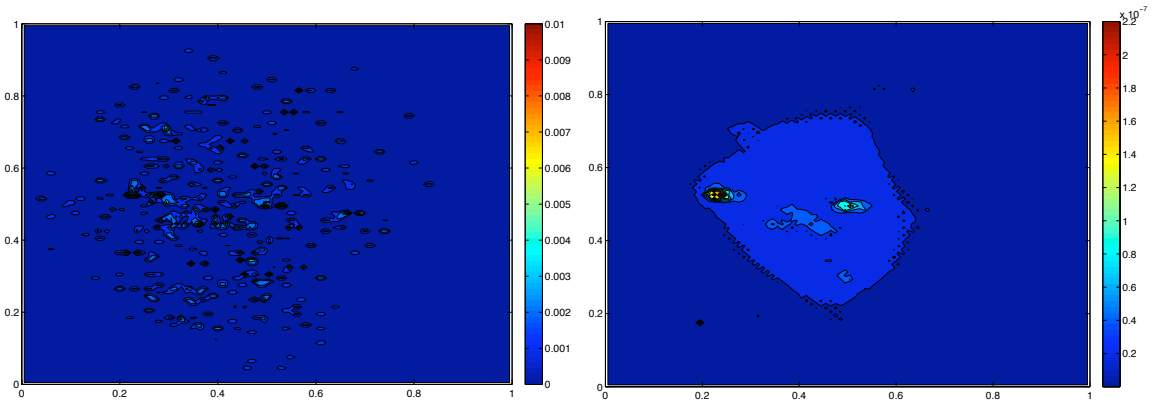

Figure 5: Left: Averaged error, $|H(x,t) - H(x,0)|$ for $t \in [0,1]$. Right: identically, averaged norm of the velocity for $t \in [0,1]$.

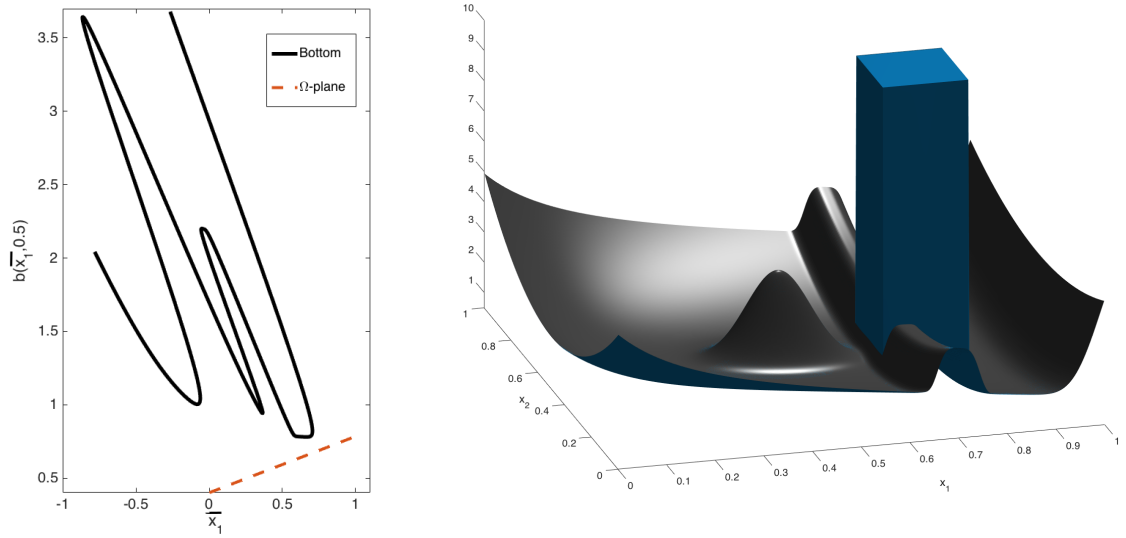

Figure 6: Left: slice of the bottom $b(\overline{x_1}, 0.5)$ with the plane of reference inclined with an angle of 20°, in *global coordinates* (meaning that $\overline{x_1}$ is obtained via the rotation associated to the angle α, see Fig. 1). Right: bottom $b(\boldsymbol{x})$ (in black) and initial condition $b + H$ (blue), in *local* coordinates.

We set $\eta = 10^{-3}\ m^2.s^{-1}$, $\tau_y = \sqrt{2}/2\ m^2.s^{-2}$, $\beta = 10^{-3}\ m.s^{-1}$ and $g = 9.81\ m.s^{-2}$. Even though b is defined analytically and it is an academic avalanche, this test is very demanding due to the high slope and the strong gradients of the bottom as well as the quantity of material in the initial column (note the strong aspect ratios in Figures 6 left and right). With these values of the parameters, the material reaches a stationary state around $t = 1\ s$, so we made simulations up to $t = 6\ s$ to check the ability of the 2D scheme to preserve this rigid free surface. This test has a rich hydrodynamics, as shown on Figures 8, 9 and 10. Recall that $V = 0$ on $\partial\Omega$. In the first phase of the collapse of the column, there are reflections (principally in the x_1 direction) on the wall at $x_1 = 1$ and on both obstacles (ridge at $x_1 = 0.75$ and Gaussian at $(x_1, x_2) = (0.5, 0.5)$) inside the domain (see $t = 0.05\ s$). This notably leads to counterwaves which collide on the ridge (see $t = 0.09\ s$ and $t = 0.11\ s$). Then, the material essentially separates in two parts on each side of the ridge and then reaches a steady state. In the upper part the material oscillates for a short time (feeding a bit the other side of the ridge), cf. $t = 0.21$ and $0.26\ s$ on Figure 9. The lower part of the material separates and goes around the Gaussian to finally meets at the bottom of the hill and reaches a stationary shape with $V \ll 1$ and H with a shape with very high gradients (after $t \approx 1\ s$, see Figures 10 and 11). It is very difficult to compute a stationary solution in this kind of configuration with wet/dry fronts but we see in Figure 11 that our scheme performs well to do so: the velocity is very small ($\|V\|_2(\Omega) = 1.5e-9$) and the level lines $\{\boldsymbol{x}|H(\boldsymbol{x}) = 0\}$ are indeed very well superposed between $t = 5$ and $6\ s$. Note that these results are computed on a mesh with 450^2 points and can be considered as converged in terms of spatial resolution. Indeed, Fig. 11d shows a mesh convergence study of the level lines $\{\boldsymbol{x}|H(t = 6, \boldsymbol{x}) = 0\}$ for various Δx. It can be seen that the results for the two more refined meshes are very close.

We also use this test to compare the AL and the BM methods in terms of numerical cost. Note that following our 1D study for BM [10, Section 3.1.3], we directly present the wet/dry front optimized version, ϖ_{opt}, of the optimal choice of the ω parameter. We proceed as follows. For both methods, we simulate from $t = 0$ to $t = 1$, with 110^2 mesh points for the Ω square, and we study the cost of the duality loops as a function of the duality parameter (we use 14 discrete values between 0.01 and 64). This cost is defined as the sum, along all the iterations in time (t^n), of the iterations of each duality loop used to compute V^n. We perform this study for four values of $\tau_y = \sqrt{2}/20,\ \sqrt{2}/2, 2\sqrt{2}$ and $5\sqrt{2}\ m^2.s^{-2}$, which are representative of 4 different dynamics of this 2D test case. Remark that we limited the number of iterations in a dual loop at 10,000 iterations: in practice, it is not reached except for the BM method at $\tau_y = \sqrt{2}/20\ m^2.s^{-2}$. Consequently this does not change the following conclusions but allows to perform this study in a more reasonable CPU time. The results are presented in Figure 7. Recall that the duality parameter is taken as a constant for all the time iterations for the AL and the standard BM. However, when optimal BM is used with the a priori derived $\varpi_{opt} = \varpi_{opt}(t)$, one can not give a meaning to the cost for a given ϖ and there is only one value of the duality cost: this leads to the horizontal lines in Fig. 7. We can see that, for this dam break problem, when τ_y increases the duality cost decreases for both AL and BM methods. Remark that the BM curve for $\tau_y = \sqrt{2}/20\ m^2.s^{-2}$ is far less convex than the other curves because, at some time iterations, it reached the maximum number of duality iterations (= 10,000) as mentioned above. But, still, we can observe an optimal value of ω, which is furthermore close to the ϖ_{opt} estimation. The AL seems to always be cheaper than the BM, especially at small τ_y. However, it can be seen that ϖ_{opt} always leads to a good estimation of the observed optimal cost and that when τ_y increases, this cost of the BM is closer to the cost of the AL. As a consequence, the optimal BM method can be very competitive w.r.t. the AL, especially at high τ_y. Indeed the optimal r for the AL method is not known a priori and the practitioner can be far from it, leading to significantly higher CPU times.

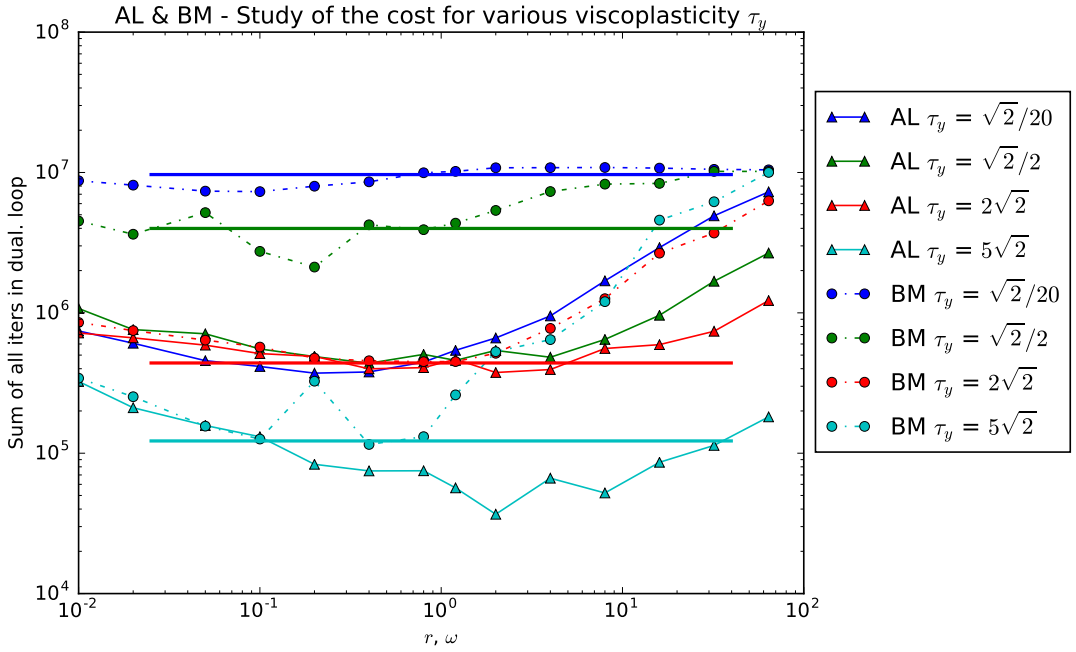

Figure 7: Duality numerical cost for four τ_y. The colored continuous curves are for the augmented Lagrangian while the dashed ones are for the standard Bermúdez-Moreno . The horizontal thick lines correspond to the cost for the BM with the optimal duality parameter ϖ_{opt} : their colors (varying with τ_y) correspond to the same colored dashed curve of the standard BM to which it principally needs to be compared; namely $\tau_y = \sqrt{2}/20,\ \sqrt{2}/2, 2\sqrt{2}, 5\sqrt{2}\ m^2.s^{-2}$ is in blue, green, red, cyan, respectively.

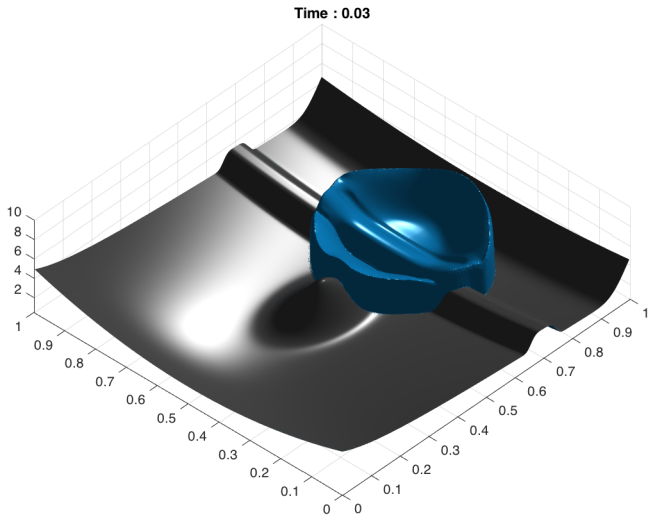

(a) $t = 0.03$

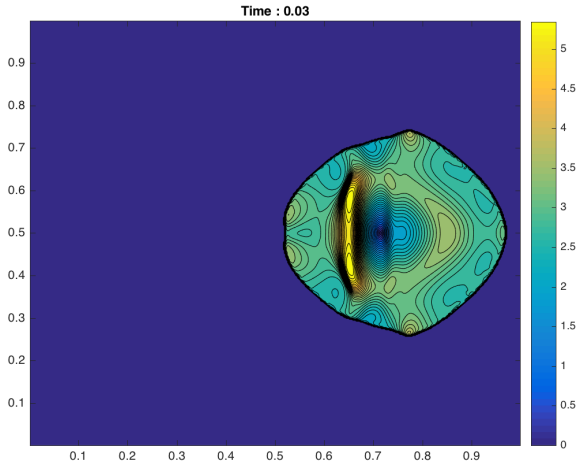

(b) $\|V\|_2(\boldsymbol{x})$, $t = 0.03$

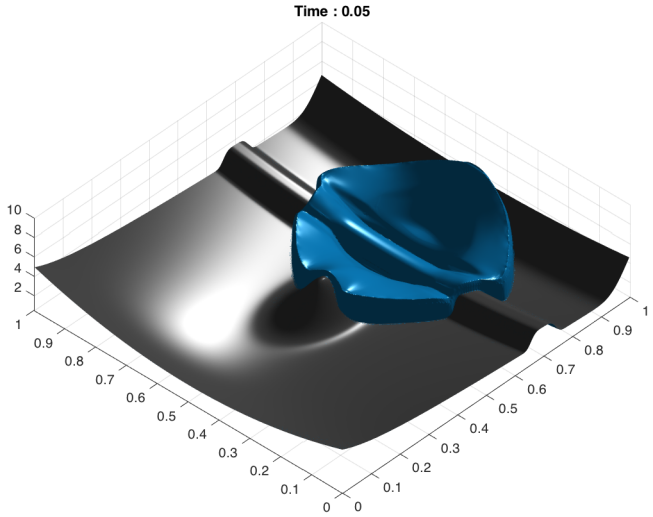

(c) $t = 0.05$

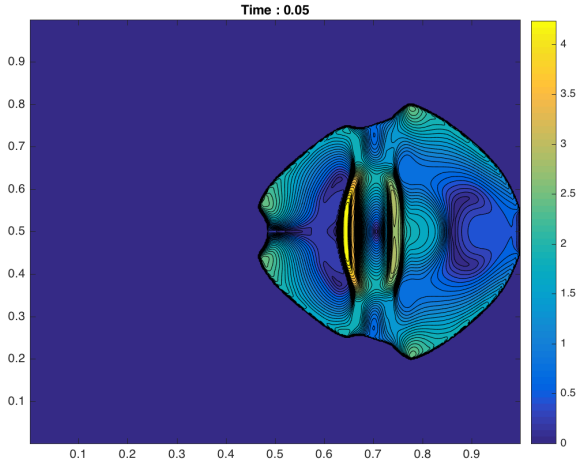

(d) $\|V\|_2(\boldsymbol{x})$, $t = 0.05$

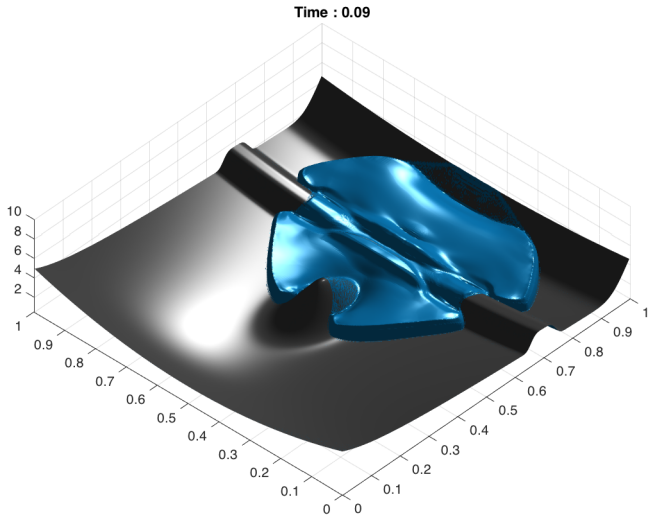

(e) $t = 0.09$

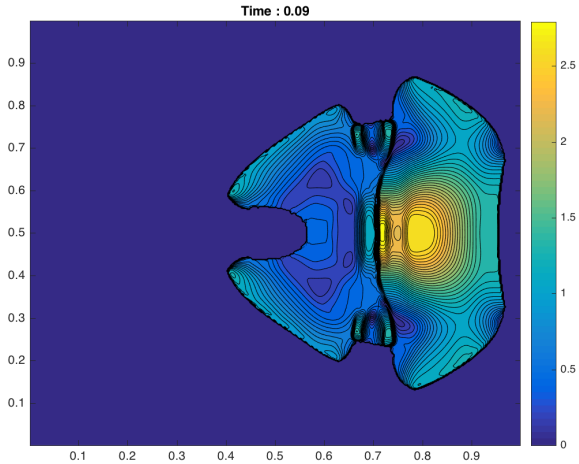

(f) $\|V\|_2(\boldsymbol{x})$, $t = 0.09$

Figure 8: Left: Free surface (blue) and bottom (black). Right: contours of $\|V\|_2(\boldsymbol{x})$. From $t = 0.03$ to 0.09.

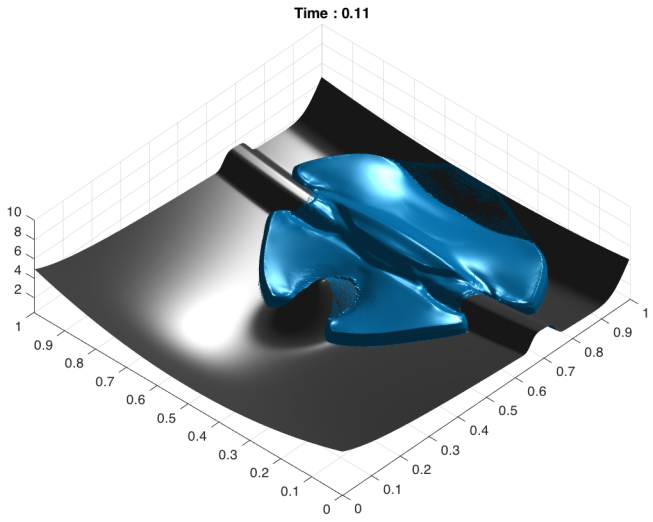

(a) $t = 0.11$

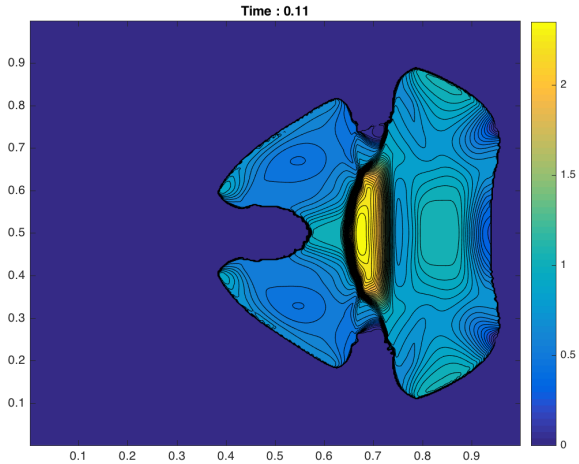

(b) $t = 0.11$

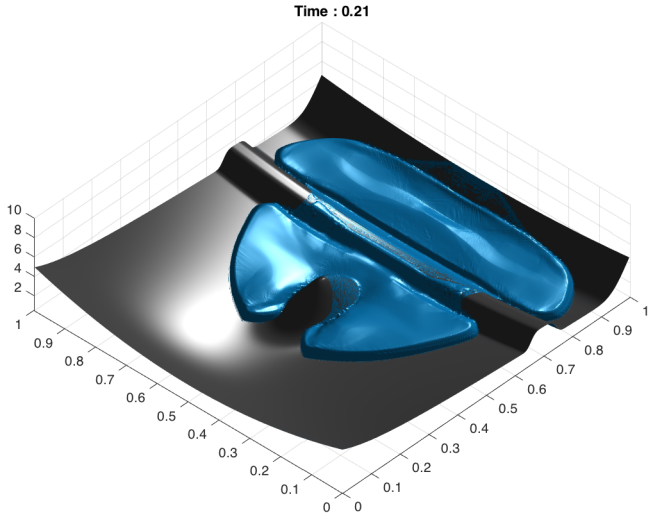

(c) $t = 0.21$

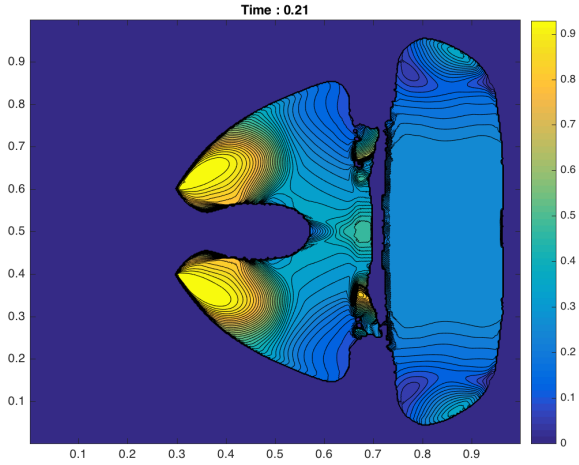

(d) $t = 0.21$

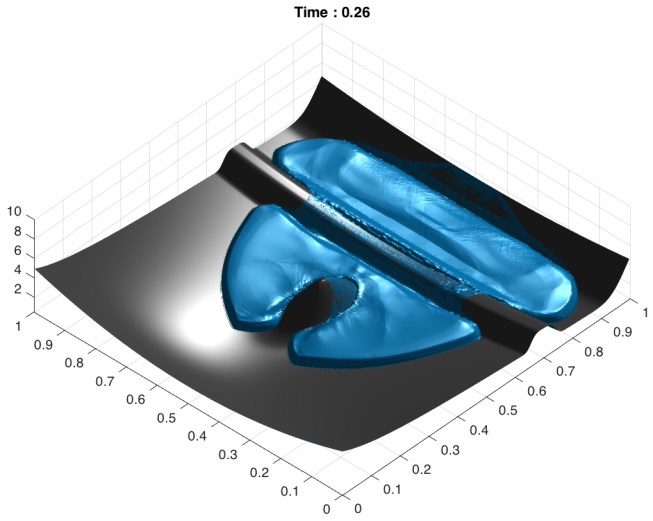

(e) $t = 0.26$

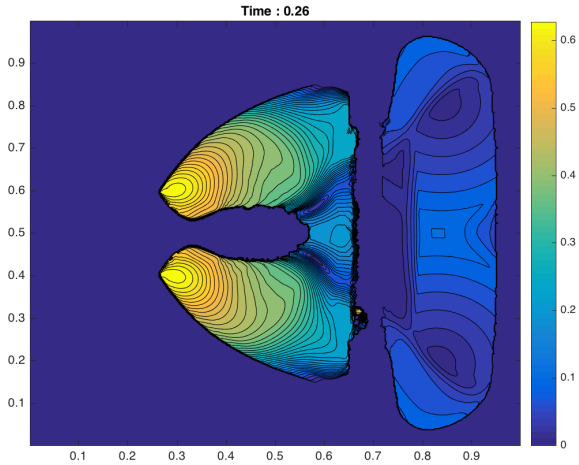

(f) $t = 0.26$

Figure 9: Left: Free surface (blue) and bottom (black). Right: contours of $\|V\|_2(\boldsymbol{x})$. From $t = 0.11$ to 0.26.

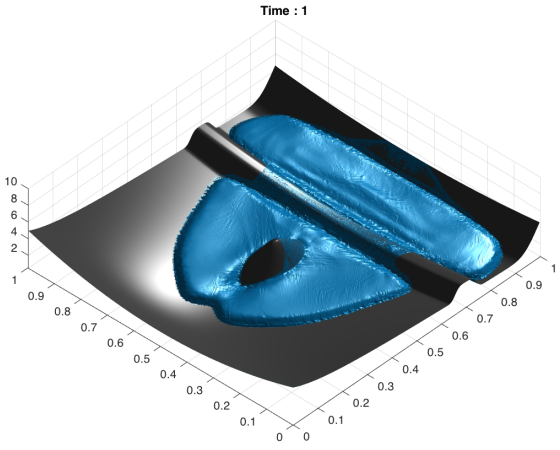

(a) $t = 1$

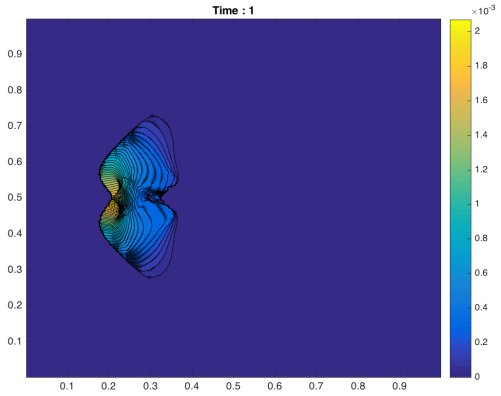

(b) $t = 1$

Figure 10: Left: Free surface (blue) and bottom (black). Right: contours of $\|V\|_2(\boldsymbol{x})$. At $t = 1$.

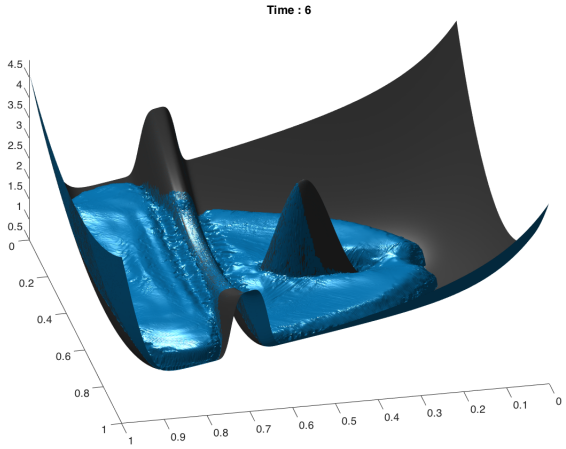

(a) Free surface at $t = 6$: rotated view to better see high gradients of H at the wet/dry front.

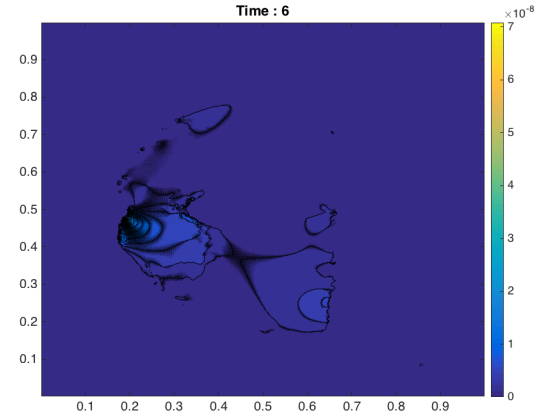

(b) Contours of $\|V\|_2(\boldsymbol{x})$ at $t = 6$. Note: $\|V\|_2(\Omega) = 1.5e-9$.

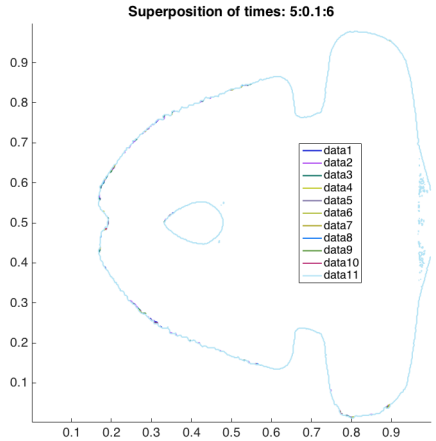

(c) Another stationary evidence. Square mesh with 450^2 points. Level line $\{\boldsymbol{x}|H(\boldsymbol{x}) = 0\}$ for different times: data$i$ for $i = 1$ to 11 stands for t from 5 to 6 with a time step of 0.1.

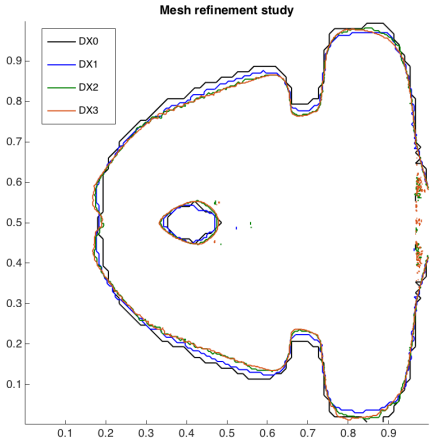

(d) Mesh refinement study: level line $\{\boldsymbol{x}|H(\boldsymbol{x}) = 0\}$ at $t = 6$ for different mesh sizes. DX0,1,2 and 3 stands for a square grid discretized with respectively 75^2, 150^2, 300^2 and 450^2 mesh points.

Figure 11: Details on the stationary state at $t = 6$ and mesh convergence study.

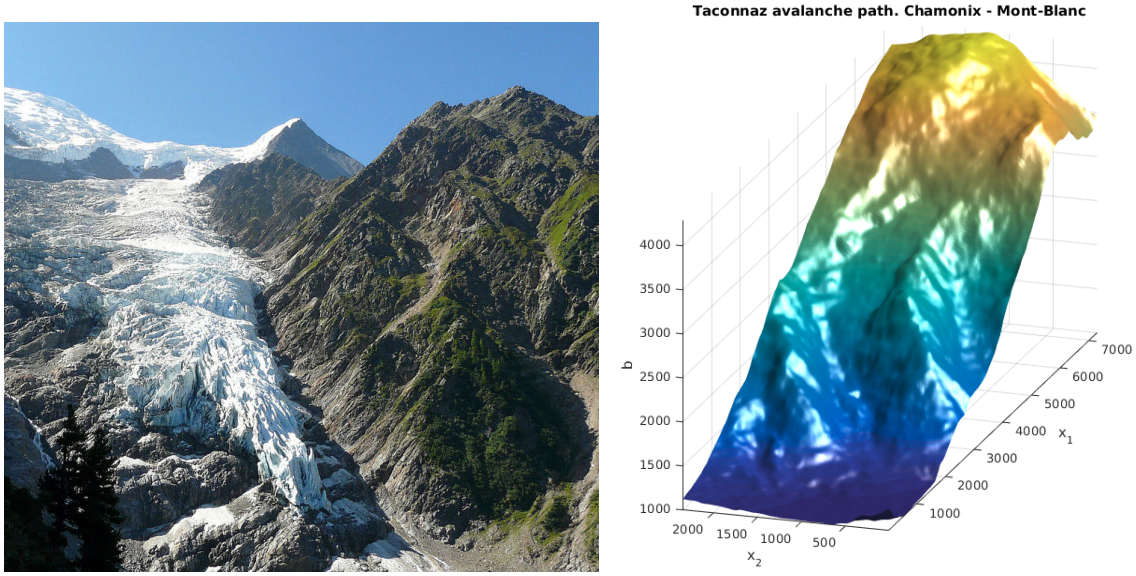

(a) Photo of the upper part of the site (Dome du Gouter on the far left and Gros Bechard on the right), courtesy [16]. Note the significant amount of ice and complexity of the terrain.

(b) Topography from ASTER GDEM: 431 × 213 mesh resolution. Dome du Gouter approximately at (6500,1600) and Gros Bechard at (3500,1000).

Figure 12: Topography of the Taconnaz avalanche path, Chamonix - Mont-Blanc.

In this section, we test the ability of the 2D numerical scheme to simulate an avalanche on a real topography. Namely, we choose the Taconnaz avalanche path in the region of Chamonix, France. This site is one of the longest in Europe with a length close to 7000 m (avalanches can start around 3300 m above sea level and stop around 1000 m a.s.l.), a width between 300 and 400 m and a mean slope of 25° (with some portions in departure areas of avalanches of mean slopes 30°). Taconnaz is well known for a significant frequency of avalanches (composed of dense and mixed snow, with speed of 70 m/s in the worst case scenario), with 75 events between years 1900 and 2000 [15].

We obtain the topography of the Taconnaz avalanche path thanks to the ASTER Global Digital Elevation Model (GDEM) v2, whose initial resolution in x_1 and x_2 is around 25-30 m [3]. For simulation purposes, we interpolate the topography on a finer grid: we built a uniform square mesh with a 16 m resolution (431×213 points in $x_1 \times x_2$), see Fig. 12. Based on historical observations [15], we put on top of this topography a truncated Gaussian of material for H whose maximal height is 9 m and volume is $0.6{\times}10^6$ m^3 (observed volumes are between $0.01{\times}10^6$ and $1.5{\times}10^6$ m^3) at an altitude of 3700 m a.s.l. on the slopes of Dome du Gouter, see Figures 13a and 13b. Namely,

$$H(t=0,\boldsymbol{x}) = \max\left(0, -2 + 11\mathrm{e}^{-(4.10^{-5})(x_1-6380)^2 - (2.10^{-5})(x_2-1050)^2}\right). \tag{55}$$

This is used as an initial condition to represent the dense snow composing the avalanche; further $V(t=0) \equiv 0$. For the material, we set $\eta = 10^{-1}\ m^2.s^{-1}$, $\tau_y = \sqrt{2}\ m^2.s^{-2}$, $\beta = 2.10^{-3}\ m.s^{-1}$, $g = 9.81\ m.s^{-2}$. Of note, for a given real observed avalanche, it is very difficult to give precise values of these parameters so we put reasonable values which lead to an observed deposit of the avalanche in the field (see [6]); in particular, we do not enforce that physical time scales are relevant, focusing only on the localization of the deposit. The objective is here to show that algorithms derived in this paper are applicable on real avalanches data to compute the stopping state. The fitting of these parameters is out of the scope of this paper and is left for future works.

The dynamics of this test, which spans from $t = 0$ to $120,000\ s$ can be decomposed in 3 phases, going to the stationary state. A first "fast" phase on a "short" time scale ($t = 0$ to approx. $3000\ s$) where the deposit reaches the bottom of Taconnaz path. The front is not stationary but it is not far from its stationary localization, see Figure 14. In a second phase, on a longer time scale (from approx. $t = 3000\ s$ to $40,000\ s$), the velocities are decreasing but there is a significant motion of the material in the whole deposit from the mountain top to the bottom: this leads to a progressive advance of the front of the avalanche. In a last "slow" phase on a much longer time (from approx. $t = 40,000\ s$ to $106,000\ s$), there is essentially no motion on the top 3/4 of the deposit and most of the material is in the 1/4 bottom part where the slope is still significant (see H on Fig. 18 (b) Bottom): as a consequence there is a slow but progressive sliding motion of this bottom part (as also shown by the time evolution of $\max_{x\in\Omega} \|V\|_2(t,x)$ on Figure 16) and the deposit front is moving a bit (compare Figs. 15 and 17) but finally stops at about $t = 106,000\ s$. We show that the front $\{\boldsymbol{x}|H(\boldsymbol{x}) = 0\}$ is completely stationary after $t = 106,000\ s$ by also showing the solution

at $t = 120,000\ s$ (Fig. 17). Note that the final shape of the deposit is very close to one of the biggest deposits shown in [6] and measured from true avalanches at Taconnaz. Our test thus covers all the topographical difficulties associated to the Taconnaz avalanche path.

It can be seen that the stationary state is very well computed: the final velocity is locally of order 10^{-10}, and globally $\|V\|_2(\Omega) \leq 4.6 \times 10^{-9}$, see Figure 17. The position of the wet/dry front is shown to be stationary with superimposed level lines $\{\boldsymbol{x}|H(\boldsymbol{x}) = 0\}$ after $t = 106,000\ s$ with a very good accuracy (it does not move up to $t = 120,000\ s$), see Figure 19. Note that the stationary state is difficult to capture since the major part of the deposit accumulates in a zone where there is a significant slope of b, see Figure 18. The viscoplastic nature of the material with a bumped surface of the deposit (H) is clearly exhibited in this stationary state. These results show the ability of present well-balanced schemes to perform accurate simulations for Bingham type materials with real topographies from digital elevation models (DEM).

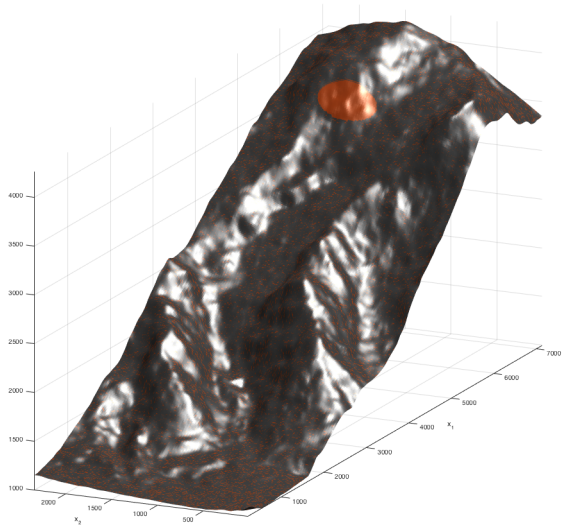

(a) topography $b(\boldsymbol{x})$ (black) and free surface H (brown).

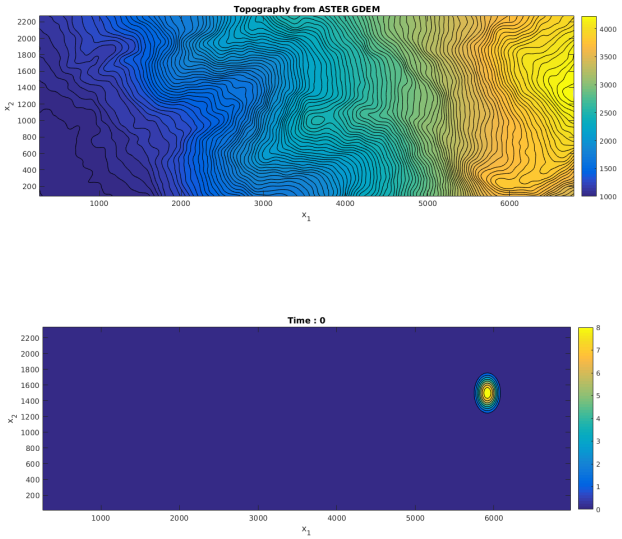

(b) filled contours of b (top) and H at $t = 0\ s$ (bottom).

Figure 13: Details on topography and initial condition of the simulation on Taconnaz avalanche path. Note that Fig. 18b gives also b together with its gradient.

6. Conclusions

In this article, we presented 2D numerical schemes in the finite volume framework which allow to compute accurately shallow viscoplastic flows: thanks to a specific design coupling duality methods and well-balancing, they preserve with a good accuracy the stationary solutions (naturally associated to the viscoplasticity) on general 2D shapes of bottom and free surfaces. These schemes deal with true wet/dry fronts and there is no need to add a small quantity of material in all the domain (as sometimes done by other methods). The well-balanced property is shown to be exact on two kinds of stationary solutions (Theorem 1). A careful study of the optimal cost of the two duality methods (Augmented Lagrangian and Bermúdez-Moreno) was performed and showed that the BM method can become competitive at high τ_y due to the fact that the optimal duality parameter is known a priori. Such studies are quite rare in the 2D framework. We finally give numerical evidence that these numerical methods can be successfully applied to real topographies as shown by the avalanche test case in the Taconnaz path obtained from ASTER GDEM. As a by-product of this study, we also provide a 2D benchmark for classic 2D Bingham codes thanks to an analytic solution with totally non-homogeneous boundary conditions on the velocity.

Acknowledgments

This research has been partially supported by the Spanish Government and FEDER through the Research projects MTM2012-38383-C02-01, MTM2012-38383-C02-02, MTM2015-70490-C2-1R and MTM2015-70490-C2-2R. Part of this work was done while P. V. was visiting E.D. F.-N. and J.M. G., during a stay in 2013 thanks to a grant from the *Instituto Universitario de Investigación de Matemáticas de la Universidad de Sevilla* (IMUS).

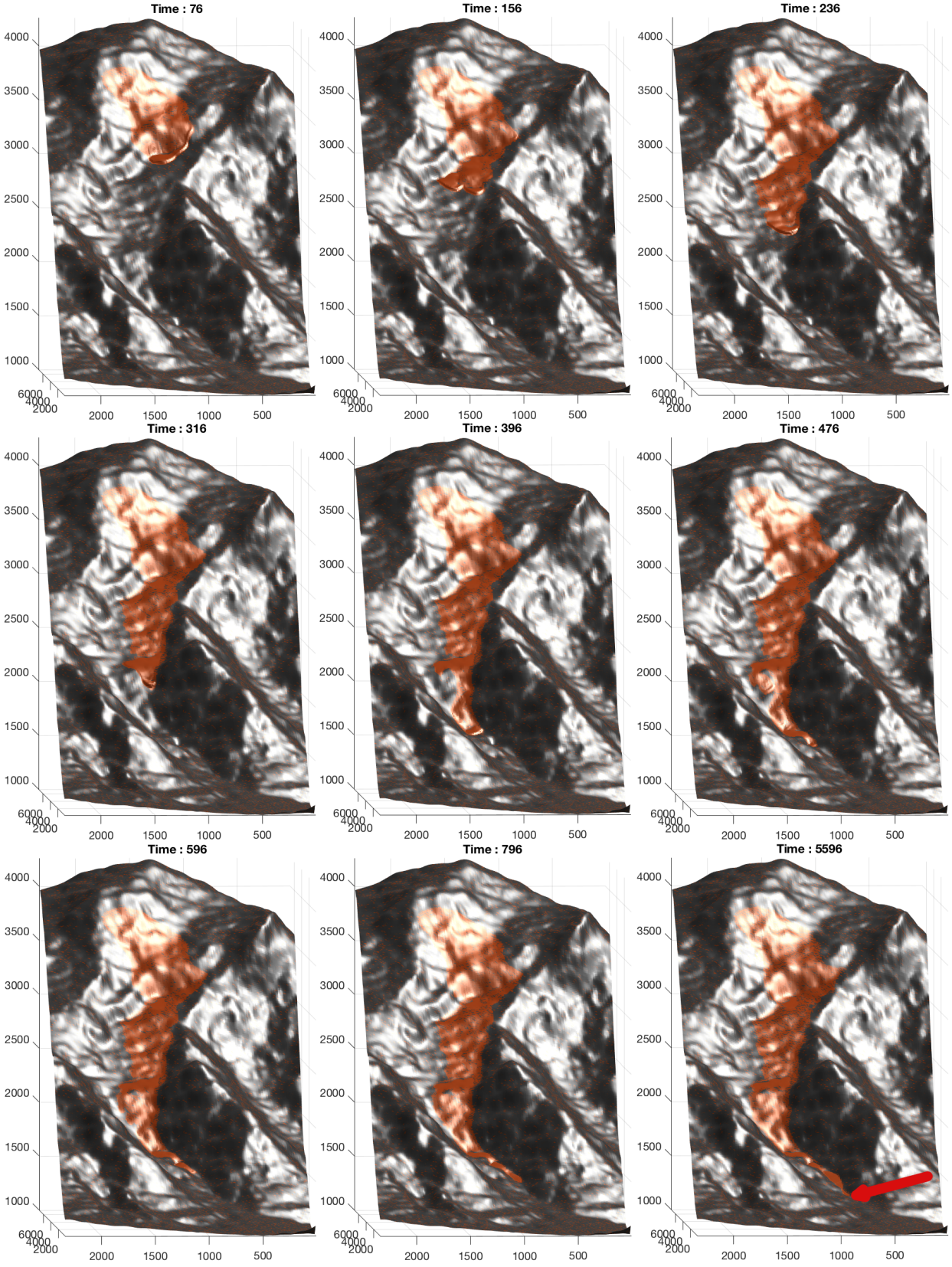

Figure 14: First times of the avalanche between $t = 76$ and $t = 5596$: topography b (black) and free surface H (brown). See also Fig. 15 for the corresponding velocities. At $t = 5596$, the red arrow shows the localization of the zoom made on Fig. 18a.

P. V. wishes to thank everyone at IMUS for their hospitality. A visit of E.D. F.-N. was supported in 2015 by the LABEX MILYON (ANR-10-LABX-0070) of Université de Lyon, within the program "Investissements d'Avenir" (ANR-11-IDEX-0007) operated by the French National Research Agency (ANR). The support of French ANR Grant ANR-08-JCJC-0104, TELLUS Grant from CNRS INSU-INSMI (2016 Call) and InFIniTi Grant from CNRS (2017 Call) is also gratefully acknowledged.

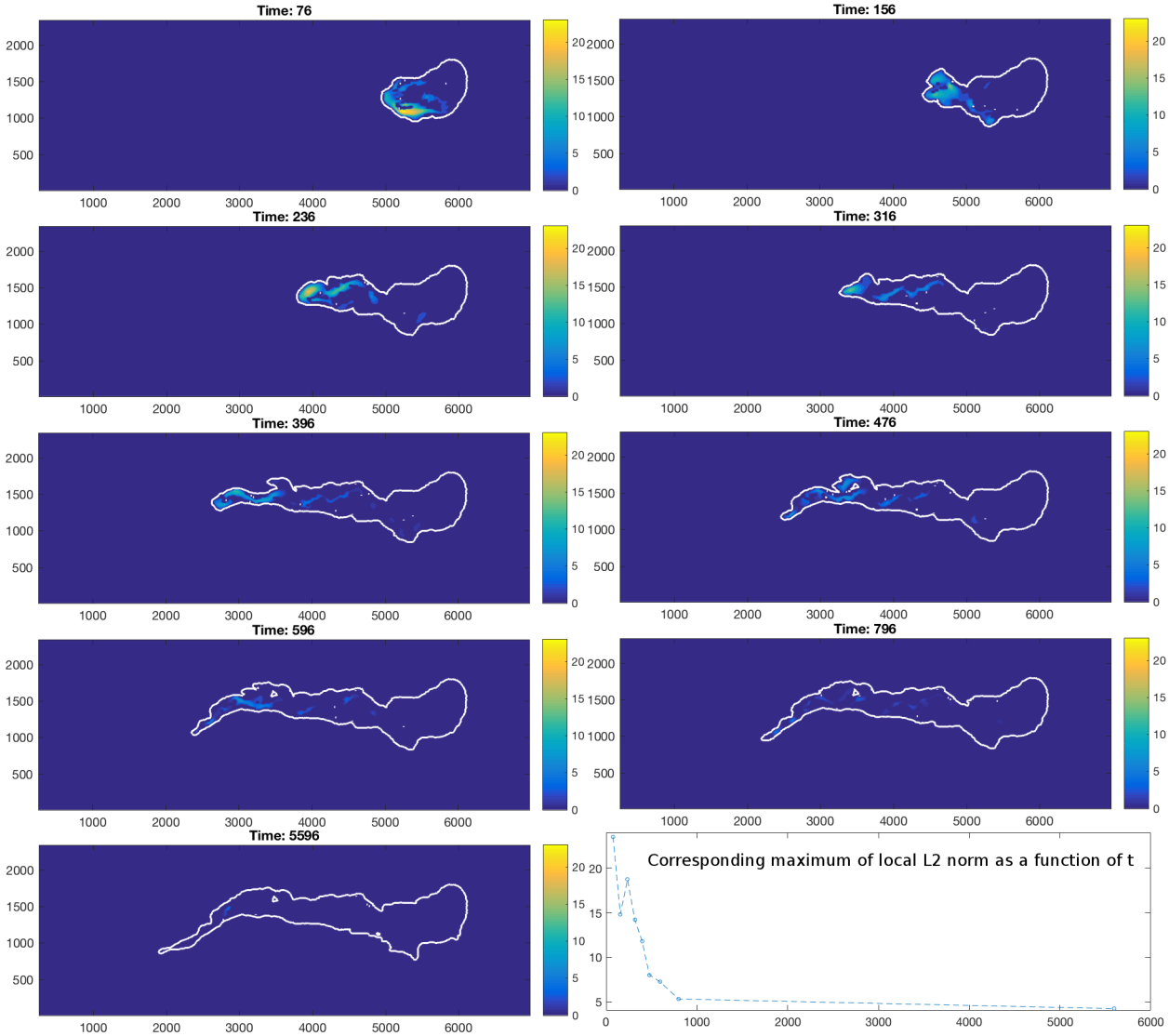

Figure 15: First times of the avalanche between $t = 76$ and $t = 5596$: $\|V\|_2(\boldsymbol{x})$ (filled contours) and level line $\{\boldsymbol{x}|H(\boldsymbol{x}) = 0\}$ (white thick line). The colorbar is the same on all snapshots so we also give, at the bottom right of the figure, the corresponding maximum values of $\|V\|_2(\boldsymbol{x})$ as a function of time. Note: at $t = 5596$, $\max_{\boldsymbol{x}} \|V\|_2(\boldsymbol{x}) = 4.22$, see also Fig. 16 for the total history. See also Fig. 14 for the corresponding 3D views of b and H.

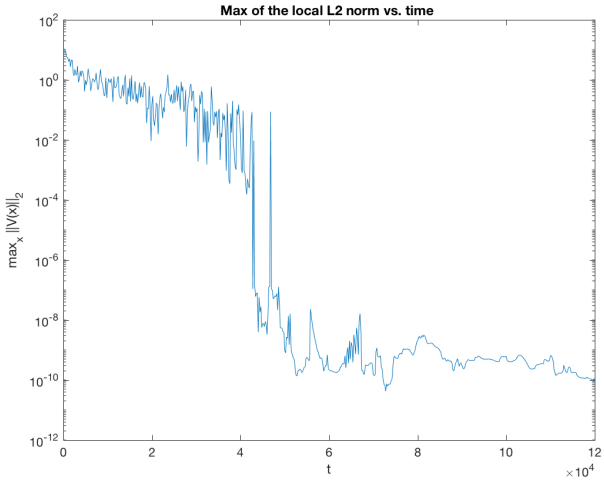

Figure 16: History of V converging to the stationary state for the Taconnaz test, in semi-log scale.

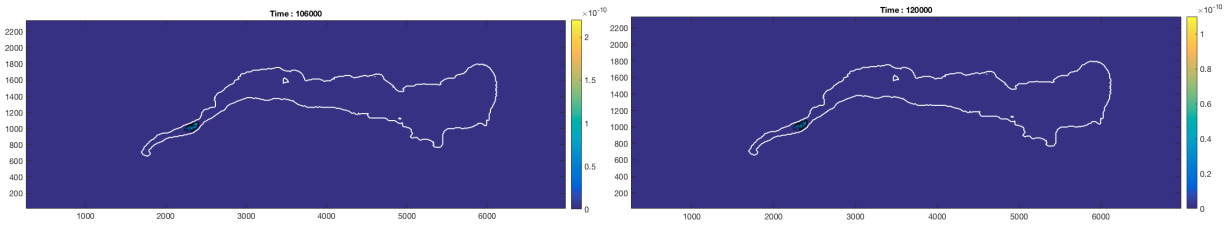

(a) $t = 106,000$ (b) $t = 120,000$

Figure 17: Reaching the stationary state of the avalanche: $||V||_2(\boldsymbol{x})$ (filled contours) and $\{\boldsymbol{x}|H(\boldsymbol{x}) = 0\}$ (white thick line). Note: $||V||_2(\Omega) = 9.0e{-}9$ at $t = 106,000$ (a) and $4.6e - 9$ at $t = 120,000$ (b).

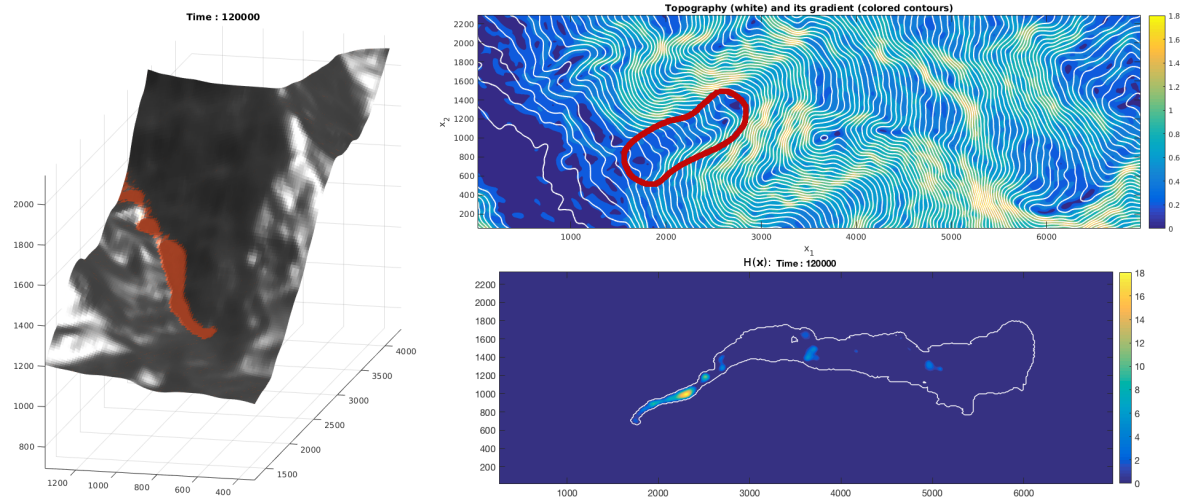

(a) Zoom (mentioned in Fig. 14) on the 3D view of $b(\boldsymbol{x})$ (black) and H (brown) at the front.

(b) Top: b with white contours and $||\nabla b||_2(\boldsymbol{x})$ with colored contours. Thick red line localize the bottom part of the deposit shown on the left (for ease of reading only). Bottom: $H(\boldsymbol{x})$ (filled contours) and $\{\boldsymbol{x}|H(\boldsymbol{x}) = 0\}$ (white line = total deposit shape).

Figure 18: Reaching the stationary state of the avalanche: $t = 120,000$, physiognomy of the deposit front and evidence of the slope of b.

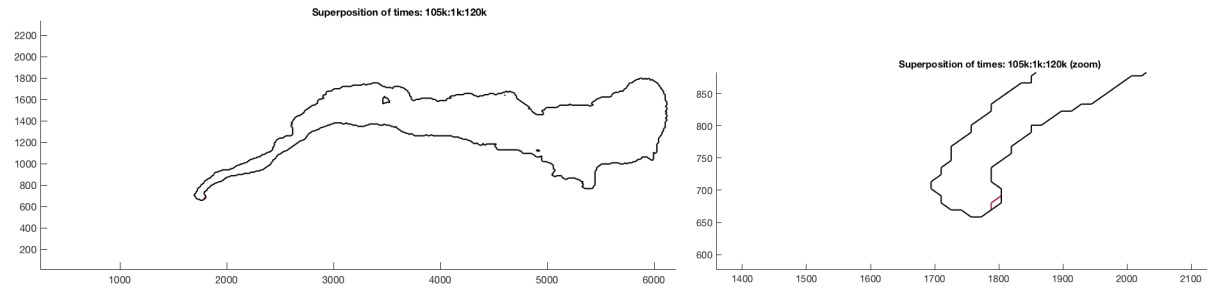

(a) Total deposit (b) Zoom on the front of the avalanche of left figure.

Figure 19: Another evidence of the stationary state: (a) levels $\{\boldsymbol{x}|H(\boldsymbol{x}) = 0\}$ from $t = 105,000$ to $120,000$ with step 1000. Two colors are seen: the red contour is $t = 105,000$, then from $t = 106,000$, all contours are superimposed and correspond to the black contour. (b) A zoom is needed to better see this small motion (of order one mesh point) between $t = 105,000$ and $t = 106,000$.

References

[1] C. Ancey. Plasticity and geophysical flows: A review. *Journal of Non-Newtonian Fluid Mechanics*, 142:4 – 35, 2007. 1

[2] Christophe Ancey and Vincent Bain. Dynamics of glide avalanches and snow gliding. *Reviews of Geophysics*, 53(3):745–784, September 2015. 1

[3] Global Digital Elevation Model v2 ASTER, 2009. Tile N45E006 is used. ASTER GDEM is a product of METI and NASA. doi: 10.5067/ASTER/ASTGTM.002. 22

[4] D. Bresch, E. D. Fernandez-Nieto, I. R. Ionescu, and P. Vigneaux. Augmented Lagrangian method and compressible visco-plastic flows: Applications to shallow dense avalanches. In G. P. Galdi et al., editor, *New Directions in Mathematical Fluid Mechanics*, Advances in Mathematical Fluid Mechanics, pages 57–89. Birkhauser Basel `http://hal.archives-ouvertes.fr/hal-00327369/en`, 2010. 2

[5] J. Cea and R. Glowinski. Méthodes numériques pour l'écoulement laminaire d'un fluide rigide visco-plastique incompressible. *Int. J. Comput. Math., Sect. B*, 3:225–255, 1972. 7

[6] CLPA: Carte de Localisation des Phenomenes d'Avalanche, 2007 - 2014. Tiles number AK68 and AJ67 are used. CLPA is a product of MEDAD, ONF and Cemagref (now IRSTEA). Publicly available at http://www.avalanches.fr/. 22, 23

[7] E. J. Dean, R. Glowinski, and G. Guidoboni. On the numerical simulation of Bingham visco-plastic flow: old and new results. *Journal of Non Newtonian Fluid Mechanics*, 142:36–62, 2007. 7

[8] G. Duvaut and J.-L. Lions. *Inequalities in mechanics and physics*. Springer-Verlag, 1976. 2

[9] Ivar Ekeland and Roger Témam. *Convex analysis and variational problems*, volume 28 of *Classics in Applied Mathematics*. Society for Industrial and Applied Mathematics (SIAM), 1999. 7

[10] Enrique D. Fernández-Nieto, José M. Gallardo, and Paul Vigneaux. Efficient numerical schemes for viscoplastic avalanches. Part 1: The 1D case. *Journal of Computational Physics*, 264:55–90, May 2014 `https://hal.archives-ouvertes.fr/hal-01011373/en` – DOI. 1, 2, 4, 6, 7, 8, 11, 12, 13, 18

[11] R. Glowinski and P. Le Tallec. *Augmented Lagrangian and operator-splitting methods in nonlinear mechanics*, volume 9 of *SIAM Studies in Applied Mathematics*. Society for Industrial and Applied Mathematics (SIAM), 1989. 5

[12] N. Kikuchi and J. T. Oden. *Contact problems in elasticity: a study of variational inequalities and finite element methods*, volume 8 of *SIAM Studies in Applied Mathematics*. Society for Industrial and Applied Mathematics (SIAM), Philadelphia, PA, 1988. 8

[13] M. P. Landry, I. A. Frigaard, and D. M. Martinez. Stability and instability of Taylor-Couette flows of a Bingham fluid. *Journal of Fluid Mechanics*, 560:321–353, 7 2006. 28

[14] Jean-Claude Latché and D. Vola. Analysis of the Brezzi-Pitkäranta stabilized Galerkin scheme for creeping flows of Bingham fluids. *SIAM J. Numerical Analysis*, 42(3):1208–1225, 2004. 28

[15] Mohamed Naaim, Thierry Faug, Florence Naaim, and Nicolas Eckert. Return period calculation and passive structure design at the Taconnaz avalanche path, France. *Annals of Glaciology*, 51(54):89–97, May 2010. 22

[16] Photo of Christian from camp2camp.org, 2009. Ref: 1310221031-1513903585.jpg, license Creative Commons CC-by-sa. 22

[17] Carlos Parés, Manuel Castro, and Jorge Macías. On the convergence of the Bermúdez-Moreno algorithm with constant parameters. *Numer. Math.*, 92(1):113–128, 2002. 29

[18] L.E. Payne and H.F. Weinberger. An optimal Poincaré inequality for convex domains. *Arch. Rat. Mech. Anal.*, 5:286–292, 1960. 8

[19] Jean-Michel Piau. Fluides non-newtoniens. *Editions Techniques de l'Ingenieur*, [ref. article : A 710], 1979. 28

[20] Markus Reiner and Rassa Riwlin. Die Theorie der Stroemung einer elastischen Fluessigkeit im Couette-Apparat. *Kolloid-Zeitschrift*, 43:1–5, September 1927. 15, 28

[21] Pierre Saramito and Anthony Wachs. Progress in numerical simulation of yield stress fluid flows. *Rheologica Acta*, pages 1–20, January 2017. 1, 8

[22] G.H. Shortley and R. Weller. Numerical solution of Laplace's equation. *J. Appl. Phys.*, 9:334–348, 1938. 28

[23] T. Treskatis, M.A. Moyers-González, and C. Price. An accelerated dual proximal gradient method for applications in viscoplasticity. *Journal of Non-Newtonian Fluid Mechanics*, 238:115–130, 2016. 8

[24] D. Vola, F. Babik, and J.-C. Latché. On a numerical strategy to compute gravity currents of non-Newtonian fluids. *J. Comput. Phys.*, 201(2):397–420, 2004. 28

[25] S. Yavari-Ramshe and B. Ataie-Ashtiani. Numerical modeling of subaerial and submarine landslide-generated tsunami waves—recent advances and future challenges. *Landslides*, 13(6):1325–1368, December 2016. 1

[26] Gangjoon Yoon and Chohong Min. Analyses on the finite difference method by Gibou et al. for Poisson equation. *Journal of Computational Physics*, 280:184 – 194, 2015. 28

Appendix A. The Couette-Bingham flow

In this appendix, we aim at evaluating the performance of our schemes with respect to the viscoplastic features of the model. We use a test inspired by the classical (Newtonian) Couette flow between two concentric rotating cylinders. From the numerical viewpoint this is a full 2D test. But thanks to the axisymmetric geometry, we can derive an analytic solution defined in 1D, in polar coordinates (r, θ). We then have a useful non-trivial test to check the precision of our implementation of the duality methods, in a 2D space configuration.

The so-called Couette-Bingham problem consists in writing the Stokes equation between two concentric rotating cylinders (see the first plot of Figure A.20) but using the Bingham law instead of the original Newtonian law. The problem is the following. Assume that a viscoplastic material of viscosity η and yield stress τ_y is between the two cylinders which are rotating at velocity v_i at $r = r_i$ (resp v_e at $r = r_e$) for the inner (resp. external) cylinder. Momentum conservation equations read (in Cartesian coordinates as in the main text):

$$-\operatorname{div}_{\boldsymbol{x}}(\sigma) = 0 \text{ with} \tag{A.1}$$

$$\begin{cases} \sigma = 2\eta D(V) + \sqrt{2}\tau_y \frac{D(V)}{|D(V)|} \text{ if } D(V) \neq 0 \\ |\sigma| \leq \sqrt{2}\tau_y \text{ if } D(V) = 0, \end{cases} \tag{A.2}$$

where $D(V) = \frac{1}{2}\left(\nabla V + (\nabla V)^T\right)$. There is no body force but the motion of cylinders leads to a shear-driven flow. In cylindrical coordinates, we can look for a velocity $V = v(r)\mathbf{e}_\theta$. As a matter of fact, the model of the main text

degenerates to this problem when $H \equiv 1$, $f = 0$, friction, body force and non-linear convective terms are cancelled. Under such assumptions, when $t \to +\infty$, the solution of the main model converges to the solution of (A.1)-(A.2). The derivation of the analytic solution was initially performed by Reiner and Riwlin [20] (with only one non-zero velocity for the two cylinders) and various formulations can be found in other more recent articles like [19], [13] and [14]. We propose here a more general algorithm to compute the (semi)analytic solution, formulated independently from the torque. This formulation is useful as a test-case for 2D viscoplastic codes with velocities given as boundary conditions.

Algorithm: Couette-Bingham flow
Input data. Geometry: r_i, r_e. Fluid properties: η, τ_y. Boundary conditions: v_i, v_e.
Step 1. Check if we are in the case of a solid body rotation or not by comparing $\frac{v_i}{r_i}$ and $\frac{v_e}{r_e}$.

- If $\frac{v_i}{r_i} = \frac{v_e}{r_e} =: \varpi$, this is a solid body rotation. All the material is unyielded and $\forall r \in [r_i, r_e]$, $v(r) = r\varpi$. The problem is fully solved.
- If $\frac{v_i}{r_i} < \frac{v_e}{r_e}$ then the stress will be **positive**; let $sg = 1$ and go to Step 2.
- If $\frac{v_i}{r_i} > \frac{v_e}{r_e}$ then the stress will be **negative**; let $sg = -1$ and go to Step 2.

Step 2. As expected in this kind of problem, when the material is not fully unyielded, we need to determine if there is a "plug" zone in the domain $[r_i, r_e]$. To do so, it is sufficient to solve numerically the following problem for $r_y > r_i$:

$$\frac{2\eta}{\tau_y}\left|\frac{v_e}{r_e} - \frac{v_i}{r_i}\right| = \left(\frac{r_y}{r_i}\right)^2 - 2\ln\left(\frac{r_y}{r_i}\right) - 1. \tag{A.3}$$

Step 3. Two situations may occur:

- If $r_y \in]r_i, r_e[$, then there is a plug zone on $[r_y, r_e]$ (on the side of the external cylinder) where $v(r) = r\frac{v_e}{r_e}$ and a yielded zone on $[r_i, r_y]$ with $v(r)$ given by (A.5) and the following definition of the velocity at $r = r_y$:

$$v_y := \frac{v_e}{r_e} r_y. \tag{A.4}$$

- If $r_y \geq r_e$, then the material is completely yielded (*i.e.* there is no plug zone) and the velocity is given by (A.5) in which (r_y, v_y) needs naturally to be replaced by (r_e, v_e):

$$v(r) = \underbrace{\frac{v_y r_y}{r(r_y^2 - r_i^2)}\left(\left[1 - \frac{r_i v_i}{r_y v_y}\right]r^2 + \left[\frac{r_y v_i}{r_i v_y} - 1\right]r_i^2\right)}_{\text{Newtonian part}} + \underbrace{sg\,\frac{2\tau_y}{\eta}\,\frac{r_y^2(r^2 - r_i^2)\ln\left(\frac{r_y}{r_i}\right) - r^2(r_y^2 - r_i^2)\ln\left(\frac{r}{r_i}\right)}{r(r_y^2 - r_i^2)}}_{\text{"Plastic correction"}}. \tag{A.5}$$

This ends the resolution of the velocity of (A.1)-(A.2).

Numerical results
In Figure A.20, we present the flow computed with our implementation for $r_i = 0.3$, $r_e = 2.0$, $v_i = 1.5$, $v_e = 2.1$, and a material such that $\eta = \sqrt{2}$ and $\tau_y = \sqrt{2}/2$. Note that in this case, there exist both a fluid zone (yielded) and a plastic zone (unyielded) in the computation domain whose interface is at $r = r_y = 1.3344$. The discretization is done with a regular 400×400 grid. The numerical and the analytic solutions are superposed, validating our implementation of the computation of plastic and fluid zones. We also performed a grid refinement study showing a convergence in L^2-norm of the computed solution towards the exact solution. It must be noted that this test case has the numerical difficulty of being posed in a cylindrical geometry which can be handled by our Cartesian implementation (thanks to a direct penalization technique with an imposed velocity for all points outside the torus) but not with the optimal order of convergence (actually we loose one order in convergence magnitude) due to the inaccuracy of the Cartesian geometry to handle curved boundaries. This is a well known fact (see e.g. [22, 26]) and one can adopt a more adapted space discretization to deal with general curved boundaries, as proposed for instance in [24] (see also [14]). Since this is not the main objective of the present paper, we do not perform such an implementation. The main point in this section is that our scheme is convergent to the 2D analytic solution. Note that for the other tests of the paper, we use square computation domains for which we recover full accuracy of the scheme as it can be seen in the main text.
Let us now describe in more details the various results of Figure A.20. The first plot illustrates the full 2D computation domain and show the numerical velocity field in the torus associated to (r_i, r_e): we can verify that the computed vector field is as expected by the analytic solution, rotationally symmetrical (independent on the angular variable θ). The colormap shows that, on a given azimuth θ from r_i to r_e, the velocity magnitude (in absolute value) is decreasing (dark brown to light brown) then increasing (light brown to black). This velocity magnitude is quantitatively described in the two following plots. Namely, the second plot gives, in Cartesian coordinates, the values

of the y component of the velocity, namely $u_y(x, y)$, on the torus. Finally the third plot, in 1D, gives the slice of the previous u_y on the axis $y = 0$ ($u_y(x, 0)$) and from $x = r_i$ to $x = r_e$ (from $x = -r_i$ to $x = -r_e$, u_y is antisymmetric and is thus not shown). Recall that here, we have $u_x(x, y) = 0$, for the first component of the velocity. There are three types of information in this plot:

- the black thick line is the exact solution (A.5);
- the colored thin lines (starting from the null function in blue) are some of the computed u_y during the duality loop: they are converging to the exact solution as expected by the theory (note, as said above, that this fact is also true on the whole 2D domain, not only on the axis $y = 0$ which is shown for ease of visibility);
- the red dashed cross is the localization of the fluid/plastic transition at $x = r_y$, with a speed $u_y(r_y, 0) = v_y = 1.4011$ given by (A.4). It can be seen that for $x \in [r_y, r_e]$, $u_y(x, 0)$ is linear and the material moves with a solid body rotation.

For completeness, we give in Figure A.21 the results of the code for two other cases which can be exhibited by the model (A.1)-(A.2), namely the completely yielded regime and the pure plug regime. Geometry and fluid characteristics are the same as in the previous paragraph (illustrated by Fig. A.20): only the values of the boundary condition are changed in order to obtain the two aforementioned regimes. We directly give the slice of u_y on the axis $y = 0$ (where $u_x = 0$) since the whole velocity field is well computed as in Fig. A.20. On the left of Fig. A.21, the boundary conditions are $v_i = 0.15$ and $v_e = 4.6$, associated to a purely yielded flow. Whereas on the right of Fig. A.21, $v_i = 0.315$ and $v_e = 2.1$ leading to a solid body rotation in the whole domain: the velocity slice is a perfect line. In both cases, the exact solution is accurately computed.

Of note, in this special Couette geometry, it is evident that the Dirichlet boundary conditions on the speed are not homogeneous (i.e. $V \neq 0$), as assumed in the theory of the two duality methods performed in this paper. While we have just seen in previous paragraphs that the augmented Lagrangian performs well even if the boundary condition is not equal to 0, it appears that the Bermúdez-Moreno method as exposed in this article is not able to converge for this Couette geometry. However, it is possible to modify the Bermúdez-Moreno algorithm in such a way it can handle non-homogeneous boundary conditions. For instance, this has been done in article [17]. However this modification is problem dependent and need to be done on a case by case basis. Since the Bingham-Couette problem with non-zero boundary condition is not the main objective of this paper, we do not perform such implementation. As a consequence, we do not present the results with the Bermúdez-Moreno method for the Bingham-Couette flow. However, in the main text, simulations are performed with homogeneous boundary conditions and it is shown that augmented Lagrangian and Bermúdez-Moreno methods give identical results for V, as expected by the theory.

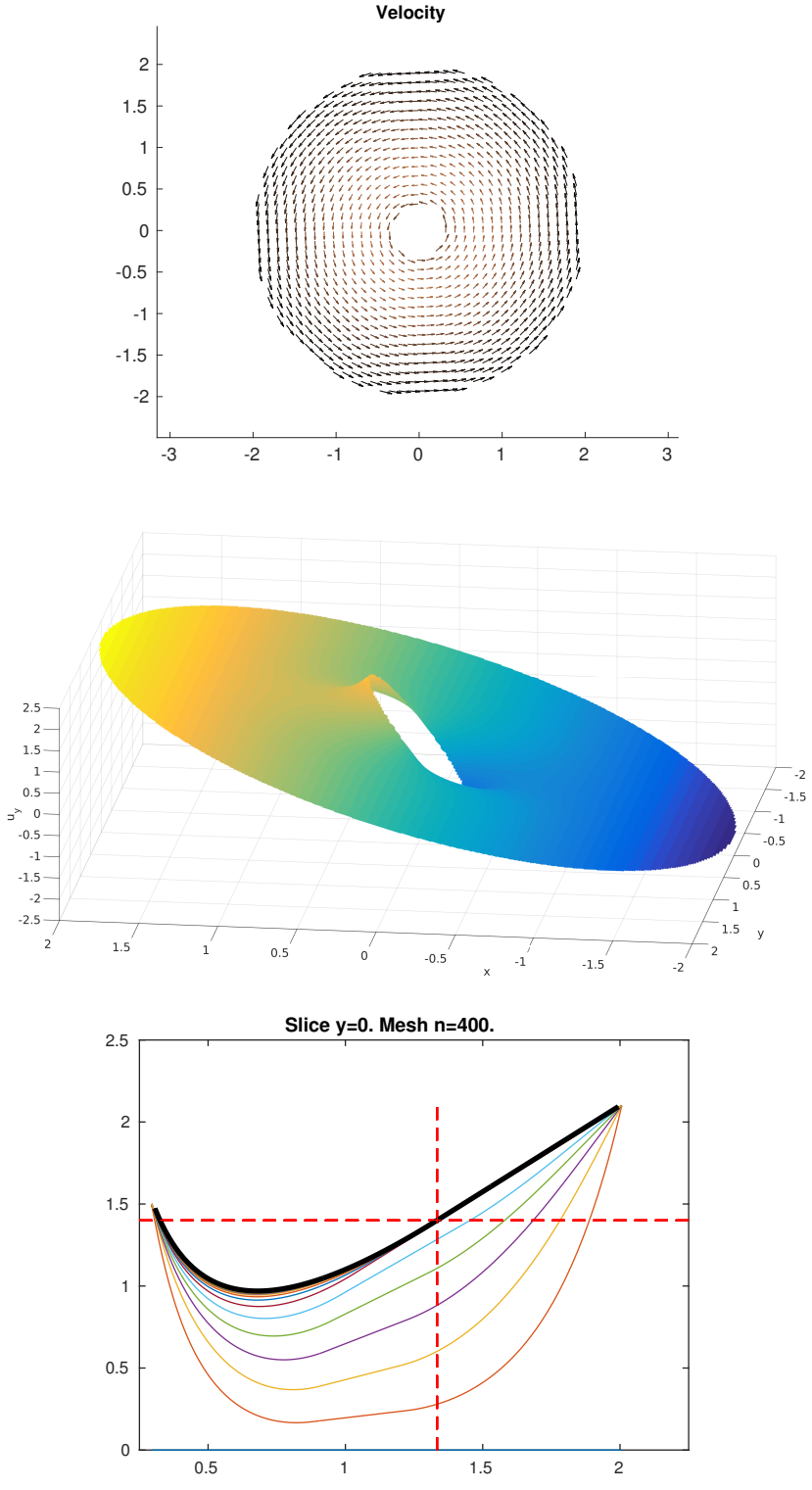

Figure A.20: Computation in 2D of the Couette-Bingham flow. See text for the value of the physical parameters and detailed description. The computational mesh contains 400^2 points. The first (quiver) plot gives the velocity field inside the two cylinders. The colormap is based on the velocity magnitude which is precised in the two subsequent plots. The second plot is the surface of the second component of the velocity, $u_y(x, y)$, on the computation domain (note that u_x and u_y are symmetric so only one of them is shown). The third plot is the slice of the same u_y on the axis $y = 0$ (where $u_x = 0$), with several curves corresponding to the evolution in the duality loop (see main text). The colored curves start with a blue zero function corresponding to the initialization of the duality loop. The colored curves then converge to the black thick line which is the exact solution given by (A.5). The convergence of the duality loop to the exact solution holds true not only graphically as in this plot but also in L^2-norm when refining the computation mesh. The red dashed cross is given here for ease of localization of the yield zone at $x = r_y$: on the left, the material is yielded whereas on the right, it is unyielded (solid body rotation).

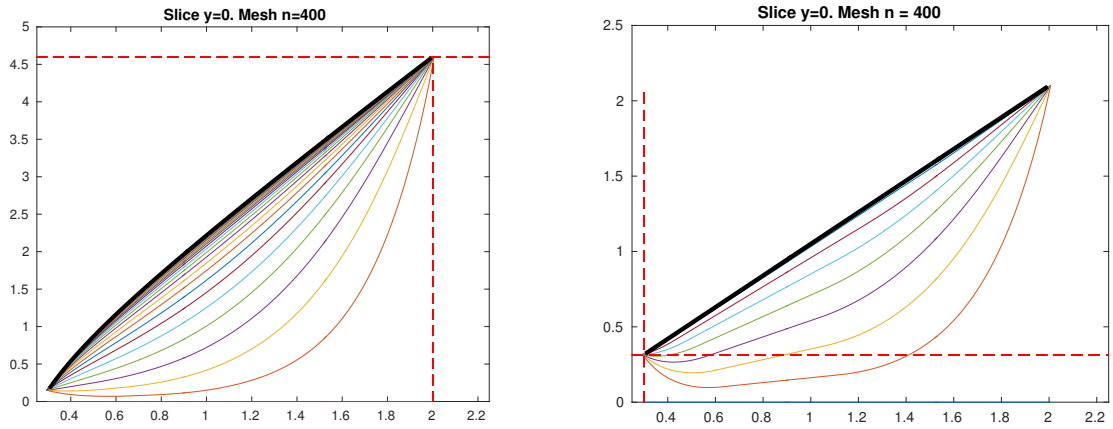

Figure A.21: Slice of u_y on the axis $y = 0$ (where $u_x = 0$), with several curves corresponding to the evolution in the duality loop (as in Fig. A.20(bottom), see also main text). The colored curves start with a blue zero function corresponding to the initialization of the duality loop. The colored curves then converge to the black thick line which is the exact solution of problem (A.1)-(A.2). The red dashed cross is given here for ease of localization of the yield zone at $x = r_y$: on the left, the material is yielded whereas on the right, it is unyielded (solid body rotation). Geometry and fluid characteristics are the same as in Fig. A.20, only the values of the boundary condition are changed. Left: $v_i = 0.15$ and $v_e = 4.6$, case of a completely yielded material (the red cross in thus exactly on the right boundary). Right: $v_i = 0.315$ and $v_e = 2.1$, case of pure plug regime (the red cross in thus exactly on the left boundary).